International Journal of
Molecular Sciences

MDPI

Article

Lorentzian-Corrected Apparent Exchange-Dependent Relaxation (LAREX) Ω-Plot Analysis—An Adaptation for qCEST in a Multi-Pool System: Comprehensive In Silico, In Situ, and In Vivo Studies

Karl Ludger Radke [1], Lena Marie Wilms [1,*], Miriam Frenken [1], Julia Stabinska [2,3], Marek Knet [1], Benedikt Kamp [1], Thomas Andreas Thiel [1], Timm Joachim Filler [4], Sven Nebelung [1,5], Gerald Antoch [1], Daniel Benjamin Abrar [1], Hans-Jörg Wittsack [1] and Anja Müller-Lutz [1]

1 Department of Diagnostic and Interventional Radiology, Medical Faculty, University Dusseldorf, D-40225 Dusseldorf, Germany; ludger.radke@med.uni-duesseldorf.de (K.L.R.); miriam.frenken@med.uni-duesseldorf.de (M.F.); marek.knet@hhu.de (M.K.); benedikt.kamp@med.uni-duesseldorf.de (B.K.); thomas.thiel@med.uni-duesseldorf.de (T.A.T.); snebelung@ukaachen.de (S.N.); antoch@med.uni-duesseldorf.de (G.A.); danielbenjamin.abrar@med.uni-duesseldorf.de (D.B.A.); hans-joerg.wittsack@med.uni-duesseldorf.de (H.-J.W.); anja.lutz@med.uni-duesseldorf.de (A.M.-L.)
2 F.M. Kirby Center for Functional Brain Imaging, Kennedy Krieger Institute, Baltimore, MD 21205, USA; stabinska@kennedykrieger.org
3 Department of Radiology, Johns Hopkins University School of Medicine, Baltimore, MD 21205, USA
4 Institute of Anatomy I, Heinrich-Heine-University, D-40225 Dusseldorf, Germany; timm.filler@uni-duesseldorf.de
5 Department of Diagnostic and Interventional Radiology, University Hospital Aachen, D-52074 Aachen, Germany
* Correspondence: lena.wilms@med.uni-duesseldorf.de

Abstract: Based on in silico, in situ, and in vivo studies, this study aims to develop a new method for the quantitative chemical exchange saturation transfer (qCEST) technique considering multi-pool systems. To this end, we extended the state-of-the-art apparent exchange-dependent relaxation (AREX) method with a Lorentzian correction (LAREX). We then validated this new method with in situ and in vivo experiments on human intervertebral discs (IVDs) using the Kendall-Tau correlation coefficient. In the in silico experiments, we observed significant deviations of the AREX method as a function of the underlying exchange rate (k_{ba}) and fractional concentration (f_b) compared to the ground truth due to the influence of other exchange pools. In comparison to AREX, the LAREX-based Ω-plot approach yielded a substantial improvement. In the subsequent in situ and in vivo experiments on human IVDs, no correlation to the histological reference standard or Pfirrmann classification could be found for the f_b (in situ: $\tau = -0.17$ $p = 0.51$; in vivo: $\tau = 0.13$ $p = 0.30$) and k_{ba} (in situ: $\tau = 0.042$ $p = 0.87$; in vivo: $\tau = -0.26$ $p = 0.04$) of Glycosaminoglycan (GAG) with AREX. In contrast, the influence of interfering pools could be corrected by LAREX, and a moderate to strong correlation was observed for the fractional concentration of GAG for both in situ ($\tau = -0.71$ $p = 0.005$) and in vivo ($\tau = -0.49$ $p < 0.001$) experiments. The study presented here is the first to introduce a new qCEST method that enables qCEST imaging in systems with multiple proton pools.

Keywords: magnetic resonance imaging; molecular imaging; CEST; qCEST; in situ; in vivo; in silico; Bloch–McConnell; IVD

check for updates

Citation: Radke, K.L.; Wilms, L.M.; Frenken, M.; Stabinska, J.; Knet, M.; Kamp, B.; Thiel, T.A.; Filler, T.J.; Nebelung, S.; Antoch, G.; et al. Lorentzian-Corrected Apparent Exchange-Dependent Relaxation (LAREX) Ω-Plot Analysis—An Adaptation for qCEST in a Multi-Pool System: Comprehensive In Silico, In Situ, and In Vivo Studies. *Int. J. Mol. Sci.* **2022**, *23*, 6920. https://doi.org/10.3390/ijms23136920

Academic Editor: Veronica Esposito

Received: 17 May 2022
Accepted: 20 June 2022
Published: 22 June 2022

Publisher's Note: MDPI stays neutral with regard to jurisdictional claims in published maps and institutional affiliations.

1. Introduction

Low back pain is one of the most common health concerns worldwide, with a lifetime prevalence of up to 80% and a huge impact on patients' quality of life and socioeconomic status [1]. Degenerative disc disease (DDD) is believed to be the main cause of low back

pain [2]. However, the underlying degenerative processes of DDD are not yet fully understood. While clinical-standard magnetic resonance imaging (MRI) is the most sensitive imaging method to assess DDD by depicting structural damage, early alterations cannot be quantified [3,4]. Consequently, more sensitive biochemical techniques are needed to assess the underlying biochemical changes that develop during the early stages of cartilage degeneration.

Chemical exchange saturation transfer (CEST) imaging has emerged as a promising bio-sensitive MRI technique alongside Na-, T1ρ-, and diffusion tensor imaging [3,5–7]. In musculoskeletal imaging, CEST has been used to assess the biochemical composition of the intervertebral discs (IVDs) [3,4,8]. The early detection of degenerative IVD alterations using CEST imaging may allow for the timely diagnosis of degenerative diseases, the initiation of targeted therapy, and a better understanding of degenerative processes. Glycosaminoglycans are an important component of the intervertebral discs and form the side chains of the complex proteoglycan molecule [9]. They are linear polysaccharides, which are composed of disaccharide units. Each of these disaccharide units has three hydroxyl and one NH group [10]. The intervertebral discs themselves consist of the collagen-fibrous annulus fibrosus and the nucleus pulposus, which is predominantly composed of proteoglycans [11]. They serve to soften shocks as well as to distribute pressure to adjacent vertebral bodies. Glycosaminoglycans are essential for this function [11].

By assessing changes in the water volume signal after selective saturation, CEST imaging is sensitive to the detection of small amounts of labile protons [12,13], and thus provides essential information that can complement conventional morphologic MRI methods. Particularly, the CEST contrast is approximately proportional to the concentration and exchange rate of the observed labile protons [14]. In fact, the measured CEST effects vary with the fractional concentration of labile protons and the exchange rate and depend on other parameters such as radiofrequency (RF) power, B_0 field strength, regional pH value, temperature, and T_1 and T_2 relaxation times [15–17].

CEST imaging techniques have further evolved over the last few years due to contributions from various technical fields, including the development of mathematical models and hardware improvement [18,19]. Furthermore, methods for the simultaneous determination of fractional concentrations and exchange rate have been introduced [17,20,21]. Based on these new methods, CEST imaging has developed into quantitative CEST analysis (qCEST) [18]. Among others, Dixon et al. indicated that the CEST effect can be plotted as a linear function of $1/B_1$ (Ω-plot) and that, consequently, the proton exchange rate (k_{ba}) from Pool B to Pool A and the labile proton ratio (f_b) of Pool B can be determined by linear regression [20]. However, this method is limited to paramagnetic CEST agents, which can be considered independent of direct water saturation (so-called spillover effect) and the magnetization transfer (MT) effect due to the large chemical shift to water [22]. For the qCEST imaging of endogenous CEST agents with smaller chemical shifts (<5 ppm), Meissner et al. proposed a novel quantitative CEST-MRI method termed AREX (apparent exchange dependent relaxation)-based Ω-plots [21]. This metric uses the MTR_{REX} calculation introduced by Zaiss et al., eliminates the spillover and MT effects, and extends it with a T_1 relaxation component [23]. However, while this approach is based on the assumption of a two-pool system, most human biochemical systems interact with more than one labile proton pool. Consequently, many studies have extended the conventional asymmetry analysis (MTR_{asym}) to a multi-Lorentzian analysis [19,24–26], allowing the separate determination of different pools' effects. Assuming that each saturation transfer and semi-solid MT signal can be approximated as a Lorentzian lineshape, these various pool effects are considered and corrected [27]. Recently, the first studies have demonstrated an increased accuracy in detecting both the MTR_{asym} and AREX signals based on multi-pool Lorentzian fits in simulations and animal tumor models [25]. Yet, to our knowledge, no prior study has used the separation of individual exchange processes via Lorentzian analysis of different B_1 values to extend AREX-based Ω-plot analysis.

Therefore, the present study aimed to (a) develop a CEST quantification algorithm applicable to multi-pool systems called Lorentzian-corrected apparent exchange-dependent relaxation (LAREX)-based Ω-plot analysis, and (b) validate the presented algorithm by in situ and in vivo experiments for several medically relevant multi-pool systems, such as amide proton transfer (APT, frequency offset Δs = 3.5 ppm) determination of the white matter in the visual cortex and histological determination of glycosaminoglycan (GAG, Δs = 1 ppm) concentration in human IVDs. Additionally, in vivo experiments are used to illustrate the transferability of the in situ results to real MR measurements. To this end, we hypothesized that (a) the AREX-based Ω-Plot method cannot be readily transferred from a two-pool system to a multi-pool system, (b) the introduced LAREX method can be used to separate the different pools and achieve comparable accuracy concerning the parameters f_b and k_{ba} as AREX in an ideal two-pool system, and (c) that conventional AREX-based evaluation cannot detect degeneration both in situ and in vivo due to the precision of different pools in human IVDs, but that these effects can be separated and subsequently evaluated using our LAREX approach.

2. Results

2.1. In Silico Study

The Bloch–McConnell simulation (please refer to Table 1 for an overview of all the parameters used) over an extended physiological range of fractional concentrations (f_b) and exchange rates (k_{ba}) demonstrated substantial differences in accuracy and feasibility between AREX- and LAREX-based Ω-plots (Figure 1). To better illustrate the accuracy of the methods and to contextualize them in the AREX-based Ω-plot in the two-pool system, Δf_b (Figure 1A) and Δk_{ba} maps (Figure 1C) were calculated with a color-coded error range of $\Delta f_b = \pm 1‰$ (Figure 1B) and $\Delta k_{ba} = \pm 300$ Hz (Figure 1D). The AREX approach did not accurately display the full analyzed range of f_b and k_{ba}. Our proposed LAREX approach allows for widely sufficient accuracy for both k_{ba} value and fractional concentration f_b determination. However, analogous to the AREX approach for two-proton pools, the exchange rate k_{ba} and the fractional concentration f_b tend to be underestimated for fast exchange rates. Similar findings were observed for our APT-qCEST models of the white and gray matter of the visual cortex (Appendix A Figures A1 and A2), our amine-qCEST model of ex-vivo blood (Figure A3), and for our creatine qCEST brain model (Figure A4).

Table 1. qCEST parameters with references for the six-pool IVD numerical simulation with solute concentration (f), the solute–water exchange rate (k_{ba}), longitudinal relaxation time (T_1), transversal relaxation time (T_2), and solute resonance frequency offset (Δ). Figure A7 also shows chondroitin sulfate as structural formula, showing the 3:1 ratio of hydroxyl to amide protons.

	Water [8]	**Hydroxyl [28]**	**Amide [25]**	**NOE #1 [25]**	**NOE #2 [25]**	**MT [25]**
Pool	A	B	C	D	E	F
T_1 (ms)	1306	$T_{1,a}$	$T_{1,a}$	$T_{1,a}$	$T_{1,a}$	$T_{1,a}$
T_2 (ms)	134	10	2	1	0.5	0.015
f	1	variable	$1/3 \times f_B$	0.003	0.007	0.1
k_{ba} (Hz)	-	variable	50	50	50	25
Δ (ppm)	0	1	3.5	−1.6	−3.5	−2.3

Abbreviations: NOE—nuclear Overhauser enhancement; MT—magnetization transfer, $T_{1,a}$—longitudinal relaxation time of the pool A, f_B—fractional concentration of Pool B.

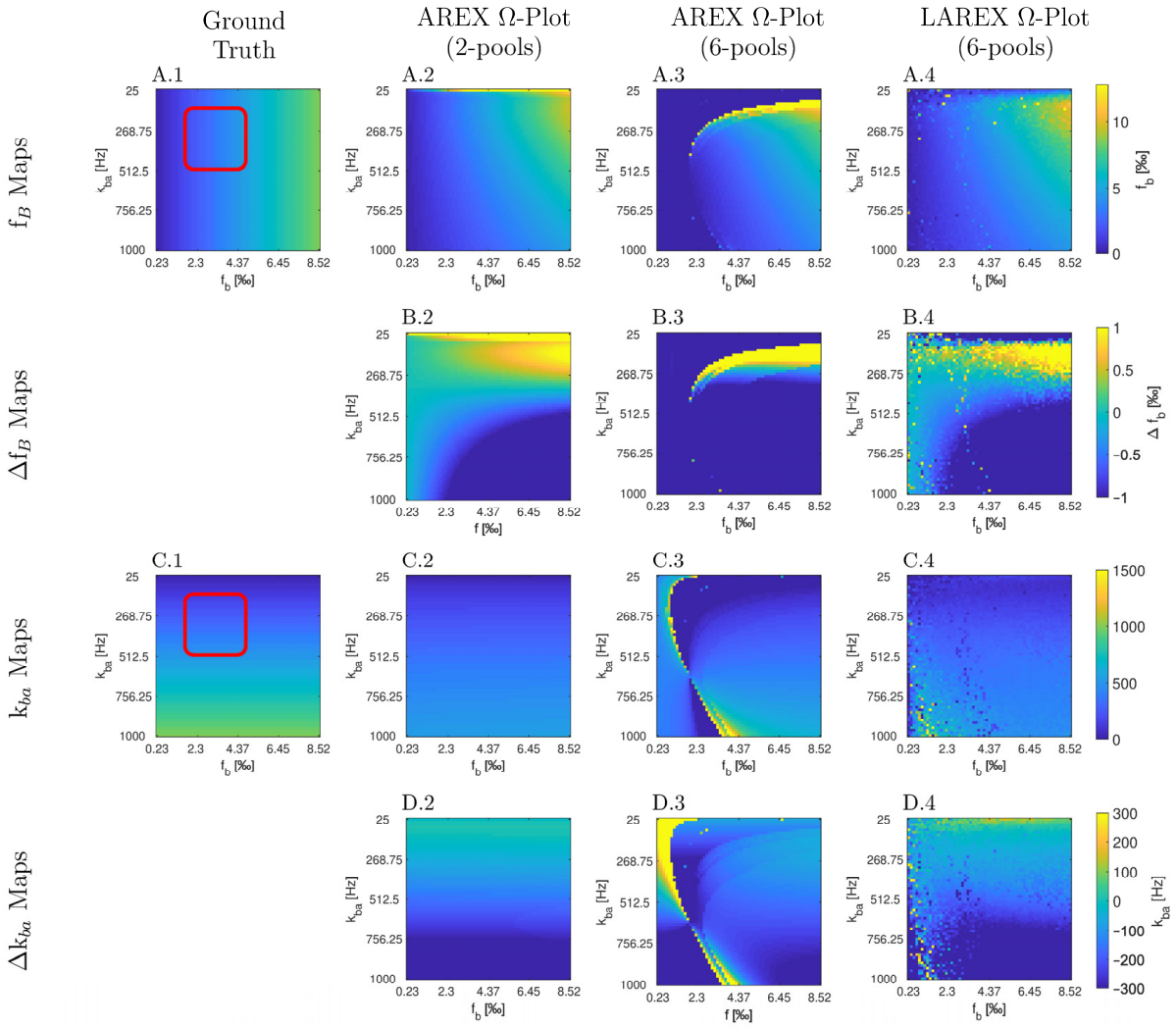

Figure 1. Parameter maps (**A**,**C**) and color-coded error maps (**B**,**D**) for fractional Glycosaminoglycan (GAG) concentrations f_b and exchange rates k_{ba}, as a function of f_b and k_{ba}, determined by apparent exchange-dependent relaxation (AREX) Ω-plots on two- and six-pool systems, LAREX Ω-plots on a six pool system, as well as the ground truth maps with a red box with marked the clinically relevant physiological range of IVD changes. The physiological parameters used are based on the exchange rates and relaxation times of human IVDs at 3 Tesla observed in previous studies [8,25,28], and are listed separately in Table 1. In this case, we only used the LAREX-based evaluation for the six-pool system because the separation of different pools characterizes this approach. The calculations are then based on the two-pool system separated in this way. Corresponding figures for further multi-pool systems investigated, such as APT qCEST imaging in the human brain, are provided in Appendix A.

2.2. In Situ Study

Ω-plots derived from eleven IVDs based on AREX and LAREX were calculated and histologically referenced. Based on the Thompson classification [29], degeneration of IVDs was quantified as follows: Grade 1 (n = 0), Grade 2 (n = 2), Grade 3 (n = 2), Grade 4 (n = 2), and Grade 5 (n = 5). In the AREX-based Ω-analysis, we did not find a significant correlation for neither fractional concentrations ($\tau = -0.17$, $p = 0.51$; Figure 2A) nor exchange rates ($\tau = 0.042$, $p = 0.87$; Figure 2B). It should be mentioned that the fractional concentration for AREX-based Ω-analysis scatter in a non-physiological range. In contrast, we observed a strong and significant decrease in f_b ($\tau = -0.71$, $p = 0.0048$, Figure 2C) and a strong but non-significant decrease in k_{ba} ($\tau = -0.58$, $p \leq 0.02$, Figure 2D) with LAREX-based Ω assessment. Furthermore, the f_B values were with f_B 0–3.5 in a physiological-range. In

comparison, we observed no significant correlations as a function of IVD degeneration for either T_1 or T_2 relaxation times.

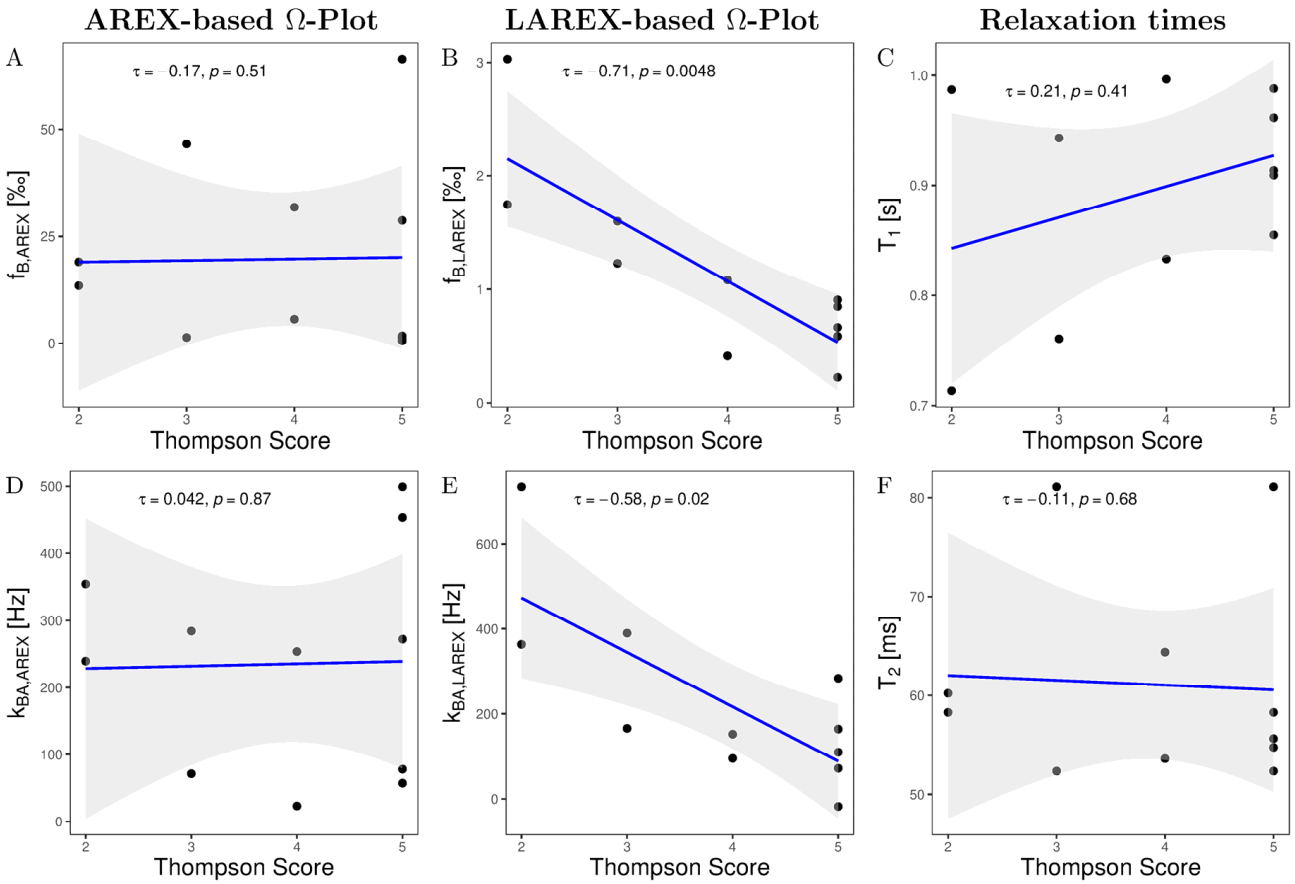

Figure 2. Kendall-Tau correlations of altered GAG fractional concentrations f_b (**A**,**B**), T_1 relaxation times (**C**), GAG exchange rates k_{ba} (**D**,**E**), and T_2 relaxation times (**F**) as a function of Thompson scoring in our measured in situ IVDs. In all correlation diagrams, a black dot corresponds to the mean value of the studied parameter for a single IVD and the gray background illustrates the 95% confidence interval of the correlation. (**A**) AREX-based fraction concentrations show a non-significant and negligible decrease with Thompson scoring. Moreover, AREX-based fractional concentrations scatter in a non-physiological range. (**B**) The LAREX-based determination shows a strong and significant decrease as a function of Thompson scoring. (**C**,**F**) Both Relaxation times show a non-significant correlation as a function of Thompson scoring. (**D**) AREX-based exchange rate determination shows no correlation as a function of Thompson rating. (**E**) The LAREX-based determination shows a strong and significant decrease as a function of the Thompson rating.

For the AREX-based Ω-plot analyses, an excellent reliability was observed for the determination of fractional concentration with ICC(3,1) = 0.99 (95% CI = 0.98–1) and ICC(2,1) = 0.98 (95% CI = 0.93–0.99). In addition, the determination of the exchange rate showed excellent agreement, respectively, with ICC(3,1) = 0.98 (95% CI = 0.98–1) and ICC(2,1) = 0.98 (95% CI = 0.98–1). Similarly, for our proposed LAREX-based Ω-plot analysis, we found excellent and good reliability with ICC(3,1) = 0.91 (95% CI = 0.76–0.97) and ICC(2,1) = 0.97 (95% CI = 0.91–0.99) for fractional concentration and ICC(3,1) = 0.97 (95% CI = 0.91–0.99) and ICC(2,1) = 0.68 (95% CI = 0.37–0.85) for exchange rate observation.

2.3. In Vivo Study

We examined 40 lumbar IVDs from eight volunteers with various stages of IVD degenerations using both the AREX and LAREX approaches. Based on the Pfirrmann classification [30], degeneration in IVDs was quantified as follows: Grade 1 (n = 14),

Grade 2 (n = 18), Grade 3 (n = 4), Grade 4 (n = 4), and Grade 5 (n = 0). The mean T_1 and T_2 relaxation times were 1.3 ± 0.1 s and 97 ± 16 ms, respectively, which are within the range for our simulations. In the AREX-based Ω analysis, we did not find a significant correlation for neither fractional concentrations ($\tau = 0.13$, $p = 0.3$; Figure 3A) nor exchange rates ($\tau = -0.26$, $p = 0.04$; Figure 3B). It should be mentioned that the fractional concentration with the Pfirrmann scoring increased from $f_{b,AREX} = 2.50 \pm 1.71$‰ (Pfirrmann score 1) to $f_{B,AREX} = 2.67 \pm 2.02$‰ (Pfirrmann score 4) (Table 2). In contrast, we observed a moderate and significant decrease in both f_b ($\tau = -0.49$, $p \leq 0.0001$, Figure 3C) and k_{ba} ($\tau = -0.48$, $p \leq 0.0001$, Figure 3D) with LAREX-based Ω assessment. Thereby, the fractional concentration decreased from $f_{b,LAREX} = 4.96 \pm 2.53$‰ in healthy IVDs (Pfirrmann score 1) to $f_{b,LAREX} = 0.78 \pm 0.26$‰ in pronounced degenerated IVDs (Pfirrmann score 4) (Table 2). Furthermore, for the in vivo experiments, we observed a significant moderate correlation to disc degeneration for both T_1 ($\tau = -0.46$, $p = 0.0002$, Figure 3D) and T_2 ($\tau = -0.5$, $p \leq 0.0001$, Figure 3D) relaxation times. An anatomical image and the corresponding calculated f_b and k_{ba} maps of a representative lumbar spine demonstrate the ability to differentiate between different stages of degeneration using the LAREX-based Ω-plot analysis (Figure 4).

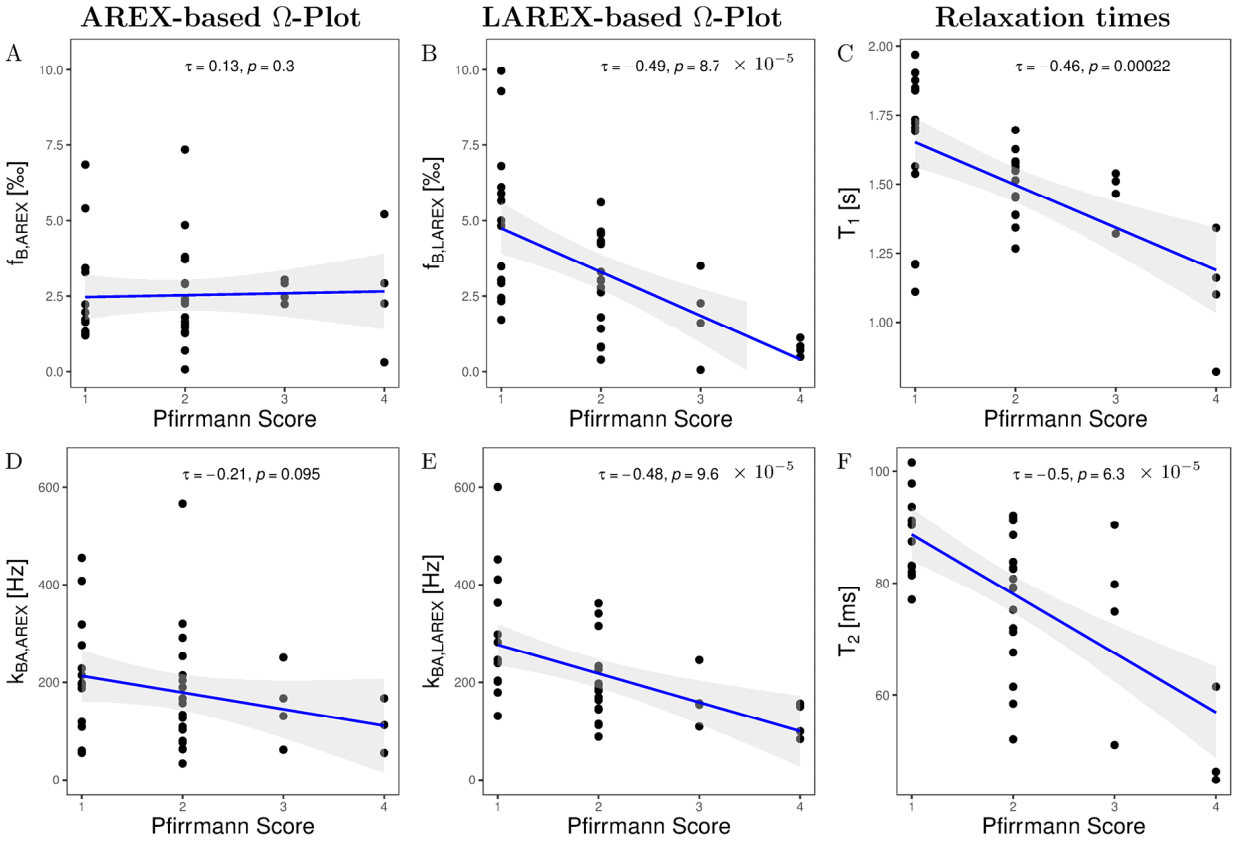

Figure 3. Kendall-Tau correlations of altered fractional GAG concentrations f_b (**A**,**B**), GAG exchange rates k_{ba} (**D**,**F**), T_1- (**C**), and T_2 relaxation times (**F**) as a function of Pfirrmann scoring in our measured in vivo IVDs and the two methods examined, the AREX-based Ω-plot and the LAREX-based Ω-plot. In all correlation plots, a black dot corresponds to the mean value of the studied parameter for a single IVD and the gray background illustrates the 95% confidence interval of the correlation. (**A**) AREX-based fractional concentrations show a non-significant and negligible decrease with Pfirrmann scoring. (**B**) The LAREX-based determination of fractional GAG concentrations shows a moderate and significant decrease as a function of Pfirrmann scoring. (**C**) T_1 relaxation times shows a moderate and significant decrease with Pfirrmann scoring. (**D**) The AREX-based exchange rate determination shows a small and non-significant increase as a function of Pfirrmann scoring. (**E**) With Pfirrmann scoring, the LAREX-based exchange rate shows a moderate and significant reduction. (**F**) T_2 relaxation times shows a moderate and significant decrease with Pfirrmann scoring.

Table 2. Evaluation of the imaging characteristics of fractional concentration (f_b) and exchange rate (k_{ba}) for the degenerative stage (Pfirrmann score). Each value is expressed as mean and standard deviation.

Parameter	Pfirrmann Score	AREX-Based Ω-Analyses	LAREX-Based Ω-Analyses
f_b [‰]	1	2.49 ± 1.71	4.96 ± 2.54
	2	2.48 ± 1.68	3.04 ± 1.52
	3	2.48 ± 1.67	1.85 ± 1.43
	4	2.67 ± 0.38	0.79 ± 0.26
k_{ba} [Hz]	1	215.7 ± 118.2	292.2 ± 125.5
	2	175.2 ± 127.1	199.5 ± 76.0
	3	152.6 ± 78.7	166.7 ± 57.1
	4	80.9 ± 76.5	122.6 ± 36.4

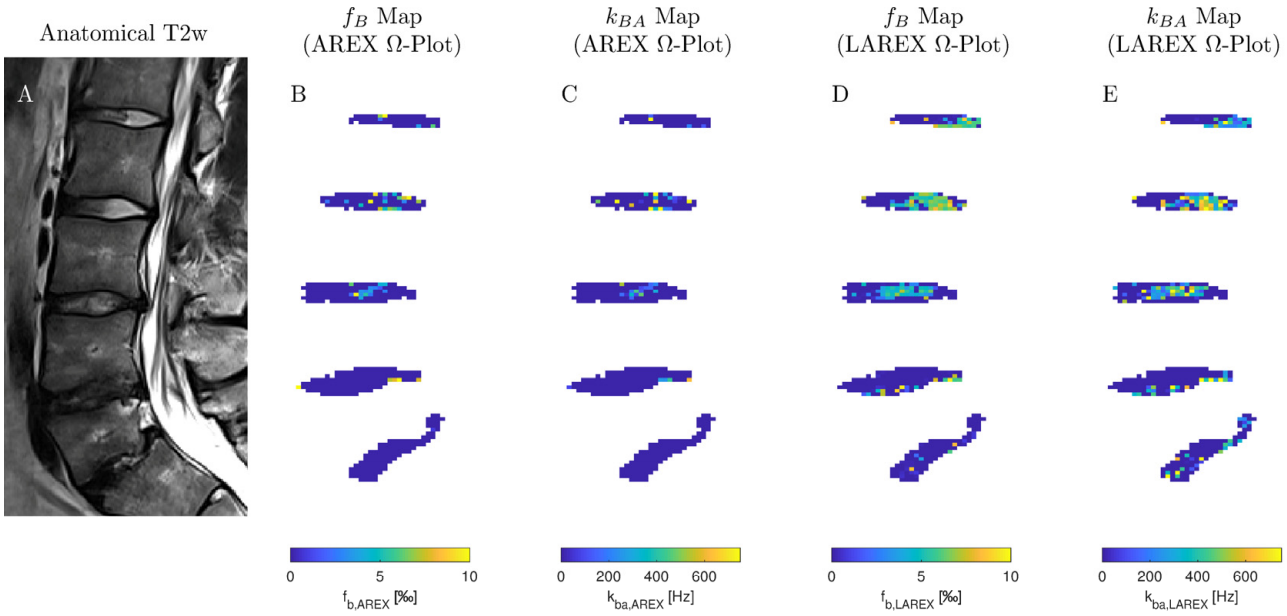

Figure 4. A sagittal image of representative IVDs and the corresponding exchange rate maps in one subject. (**A**) T2-weighted image in the sagittal plane (Pfirrmann scores from head to feet: 2, 2, 3, 4, and 4). (**B**,**C**) Exchange rate maps of the corresponding IVDs using the AREX method. (**D**,**E**) The related exchange rate maps using our proposed LAREX-based Ω-plot method. Figure A6 additionally attaches the T1 and T2 maps as well as a B0 map for the volunteer shown in this figure.

For the AREX-based Ω-plot analyses, an excellent reliability was observed for the determination of fractional concentration with ICC(3,1) = 0.94 (95% CI = 0.90–0.96) and ICC(2,1) = 0.95 (95% CI = 0.91–0.97). In addition, the determination of the exchange rate showed good and excellent agreements, respectively, with ICC(3,1) = 0.87 (95% CI = 0.78–0.92) and ICC(2,1) = 0.95 (95% CI = 0.92–0.97). Similarly, for our proposed LAREX-based Ω-plot analysis, we found good reliability with ICC(3,1) = 0.75 (95% CI = 0.61–0.84) and ICC(2,1) = 0.88 (95% CI = 0.81–0.93) for fractional concentration and ICC(3,1) = 0.85 (95% CI = 0.74–0.91) and ICC(2,1) = 0.78 (95% CI = 0.63–0.87) for exchange rate observation.

3. Discussion

This study demonstrates the feasibility of qCEST using a new LAREX-based Ω-plot approach to study fractional concentration in a multi-pool system. We validated our proposed LAREX-based Ω-plot approach for GAG concentration, in silico, in situ (human IVDs from body donors), and in vivo (using IVDs from volunteers). In addition, we have demonstrated the applicability of our method using in silico experiments for APT-

qCEST imaging in the brain, amine-qCEST imaging of human blood, and creatine-qCEST analysis in the human brain, considering additional exchanged proton pools in Appendix A. The results indicate that our proposed method substantially improves the accuracy of determining the fractional concentration and the exchange rate.

In contrast to morphological MRI, compositional MRI quantifies tissue composition beyond mere morphology and structure. However, human tissues are complex biochemical systems consisting of numerous components. Thus, while tissue composition can be adequately quantified using compositional MRI, alterations of a specific metabolite within the tissue are far more difficult to assess. Consequently, simple analysis methods like classical MTR_{asym} analysis or quantitative AREX-based Ω-plot analysis reach their limits here. In contrast, our introduced LAREX-based Ω-plot approach overcomes these challenges and allows for the separate analysis of the tissue's individual functional groups.

We were able to demonstrate that the presence of additional proton pools hampered the classical qCEST approach based on an AREX-based Ω-plot analysis and showed substantial deviations. Our simulations for IVDs showed that AREX substantially and systematically underestimated the fractional concentrations. This occurs in the physiological range from f_B = 0.5–5‰ and k_{sw} = 100–500 Hz for the GAG-OH pool, which is clinically relevant. Comparable results were observed by Zhou et al. [31] in a comparison of ideal two-pool phantoms and in situ IVDs. In their study, systematic deviations between in vitro and in situ experiments as a function of pH values were also observed, which were attributed to the non-analyzed pools. In contrast, the LAREX-based evaluation allows for accuracy comparable to that achieved with an ideal system consisting solely of two pools. In addition, we validated the LAREX method by in situ experiments for the quantitative assessment of APT in white and gray matter, the quantitative assessment of amines in human blood, and the assessment of creatine in the brain (Appendix A). Here, we observed comparable results for IVDs. Thus, in future studies, multi-pool methods can be analyzed equivalently using the LAREX approach to two-pool systems. The simulations used in the Appendix A were performed at a field strength of 7T. With the help of the simulations we performed, the LAREX approach we proposed could be successfully validated at 3T (in silico IVD study) and 7T (studies in the Appendix A).

In the in situ experiments, we observed that the AREX-based Ω-plot approach specifically for the determination of fractional concentration did not yield physiological results, and the results analogous to the T_1 and T_2 measurements showed no correlation to the histological scoring. Using the LAREX-based Ω-plot approach, we observed a strong and significant correlation ($\tau = -0.71$ $p = 0.005$) of fractional GAG concentration to the histological reference and lowered fractional concentrations compared to the subject collective. Studies of our group demonstrated an age dependence for the MTR_{asym} effect [32]. Since the classical AREX method is based on the MTR_{asym} under different B_1 field strengths, a decrease in the GAG-induced MTR_{asym} effect such as advanced age leads to an increase in the influence of noise and the other pools. In particular, the NOE#1 effect at −1.8 ppm significantly affects the evaluation of GAG OH protons at one ppm. This may lead to non-physiological results for IVD of advanced age (age of body donors for the in situ measurements: 88.6 ± 8.7 years). The LAREX-based approach allows, due to the Lorentzian correction, not only for the correction of other pools but also a smoothing of the Z-spectrum optimized for CEST experiments [33], which makes this approach suitable for low fractional concentrations. However, it should be considered that Lorentzian analyses have a number of 3 × n (n = number of assumed pools) free parameters. Moreover, CEST exchange problems are nonlinear, which results in the optimization function having not only one minimum but several local minima. If the initial values are chosen unfavorably compared to the input parameters, jumps between minima may occur. However, this is primarily relevant for artificially generated data with only one evaluated pixel. For in situ or in vivo measurements, this effect is compensated by the slight differences between the local pixels and the number of acquired pixels.

In the in vivo experiments performed using the LAREX approach, we observed a moderate and significant decrease in both the fractional concentration ($\tau = -0.49$, $p \leq 0.0001$) and the exchange rate ($\tau = -0.48$, $p \leq 0.0001$) of GAGs depending on the IVDs' degenerative stage. The AREX-based evaluation, on the other hand, showed no significant correlations and determined a non-physiologically increase in GAG concentrations with progressive degeneration. With LAREX, a fractional concentration of 4.96 ± 2.54‰ was observed in IVDs without any degeneration (Pfirrmann grade 1) and 0.78 ± 0.26‰ in IVDs with advanced degeneration (Pfirrmann grade 4). Considering three exchanging OH protons at one GAG [10] and a water concentration of about 80% in IVDs [34], the corresponding concentrations are 150 mM (Pfirrmann grade 1) and 25 mM of GAG concentration (Pfirrmann grade 4). Iatridis et al. determined GAG concentrations of 250 µg ± 134 GAG/mg dry IVD tissue [34], which relates to a 50–150 mM GAG concentration, which is consistent with our results. Moreover, in our in vivo experiments, we observed about two times higher fractional concentrations than in the in situ experiments, which agrees with previous studies [10,35], which showed a decrease in GAG as a function of age and associated progression of IVD degeneration. Furthermore, in previous studies, 66–100 mM GAG concentrations were found in articular cartilage [10,35]. Therefore, the cutoff and baseline values of the Lorentzian analysis we presented could be adopted to examine articular cartilage for alterations in GAG concentration in future studies. Moreover, regional differences in healthy IVDs were observed in our in vivo experiments (Pfirrmann ≤ 3, Figure 4), which might be due to the differences between nucleus pulposus and annulus fibrosus. Previous studies have also observed these regional differences using MTR_{asym} [3,4,32].

Numerous previous studies have demonstrated the potential for deep learning in medical imaging and post-processing [36–38]. Among others, Zaiss et al. showed the potential for deep learning in qCEST imaging [39]. Recently, Huang et al. published two fast and accurate ways to generate CEST/AREX contrast maps using DeepCEST and DeepAREX in animal experiments [40]. Based on those studies and our results, neural networks could be developed to eliminate the influence of other pools. Thus, our results suggest a promising new approach to qCEST imaging. Further longitudinal studies could periodically examine subjects or animal models to determine if the early deterioration can be detected.

However, our study has some limitations. First, the long measurement time of 84:35 min (in situ) and 36:15 min (in vivo) for a one-slice sequence must be mentioned. This is foremost because regular CEST experiments require long TR times, thus guaranteeing T_1 relaxation time decay. In addition, qCEST analysis requires an RF saturation time (10 s in our study) to reach a steady-state and at least three different CEST experiments with different B_1 amplitudes to perform the Ω-plots. By using dual-gradient echo strategies [41], simulated multi-slice gradient echo (GRE) sequences [42], phase-shifted multiplanar CEST—fast imaging with steady-state free precession (FISP) sequences [43], ultrafast one-shot acquisition [44], compressed sensing [45], and other imaging techniques, this limitation could be addressed in future studies [46]. Second, the two IVD MR studies we performed (in situ and in vivo) have only limited comparability. As these experiments were conducted at different temperatures (20 °C in situ and 37 °C in vivo), there may be systematic differences between the experiments due to temperature differences, which might affect the accuracy of LAREX and AREX. However, it should be noted that temperature changes do not change the linear dependence of the CEST effect on concentration [13]. Therefore, the increased accuracy of the LAREX approach compared to the AREX approach would not change by adjusting the temperature. Third, the present method relies on the fact that Lorentz functions can describe the various CEST effects. Previous studies have shown that Lorentz functions cannot represent rapidly exchanging metabolites [47]. Therefore, the accuracy of the LAREX method depends on the exchange rate of the metabolites of the multi-pool system, and as a result, LAREX is not necessarily better than AREX for all CEST metabolites [47]. Fourth, the application of the Lorentz fitting not only enables a reduction of the spurious effects of other pools but also has a CEST adaptive denois-

ing effect. Contrary to this, the AREX-based application only used the NLM denoising filter [48], which is not optimized for CEST. Fifth, our in situ assessments were only semi-quantitative concerning GAG concentrations. Recently, Kubaski et al. demonstrated a rapid, sensitive, and accurate measurement of GAG and all isomers by mass spectrometric detection analysis [49]. Thus, in the subsequent studies, the sensitivity of the LAREX approach could be investigated in more detail than the laborious spectroscopic methods. Sixth, the in situ and in vivo studies we performed were performed at only a single time point. In further studies, detailed reproducibility measurements and longitudinal studies over a long period of time are needed to detect degenerative processes at multiple time points and to investigate the degenerative changes. Seventh, in the in situ and in vivo studies we performed using LAREX, we observed a moderate change in k_{ba} as a function of the Pfirrmann grade. Previous studies have shown that pH changes in the IVD due to degeneration [31,50]. Subsequent in situ or in vitro studies will need to infer changes of k_{ba} as function of pH-values. Eighth, the application of the LAREX approach at 7T and its use outside IVDs were validated in our study only by in silico experiments. Further in situ and in vivo studies, guided by the IVD studies we performed, are needed to validate the promising LAREX approach further and prepare it for clinical applicability.

4. Materials and Methods

4.1. Study Design

This prospective feasibility study included sequential in silico, in situ, and in vivo CEST MRI assessments and was, thus, conducted in three consecutive steps: (1) implementation and validation of the novel LAREX approach for quantitative multipool CEST-MRI evaluation based on a Lorentzian adaptation and AREX-based Ω-plot analyses using in silico studies (2) evaluation of the newly implemented LAREX approach using in situ experiments and histological referencing of GAG content in human IVDs, and (3) demonstration of the in vivo applicability in eight subjects with different stages of DDD.

Written informed consent was obtained from all body donors as well as all volunteers. The study was approved by the local ethics committee (Ethics Committee of the Medical Faculty of Heinrich Heine University, Düsseldorf, Germany, study numbers: in situ 2021-1528 and in vivo 2019-551).

4.2. MR Imaging

All MRI measurements were performed on a clinical 3T MRI scanner (MAGNETOM Prisma, Siemens Healthineers, Erlangen, Germany) with a dedicated 15-channel knee coil (Tx/Rx Knee 15 Flare Coil, Siemens Healthineers) for the in situ experiments or with the integrated 24-channel spine coil (Spine Matrix coil, Siemens Healthineers) for the in vivo experiments.

For morphologic reference imaging, a sagittal T1-weighted (T1w) turbo spin-echo (TSE) sequence for the alignment of the compositional sequences as well as a sagittal T2-weighted (T2w) TSE sequence were used. For bio-sensitive MRI, T_1 and T_2 mapping sequences, as well as CEST sequences, were obtained; for T_1 mapping, an inversion recovery TSE sequence with seven inversion times (TIs: 25–3000 ms) (Table 3), while for T_2 mapping, a spin-echo (SE) sequence with 20 different echo times was obtained (TEs: 9.7–194 ms) (Table 3). Furthermore, seven (in situ) or three (in vivo) CEST sequences with different high-frequency pulse amplitudes (B_1) were acquired (Table 3). The saturation module of our CEST sequence used Gaussian RF pulses. To this end, a total of 64 saturated images were acquired at different saturation frequencies around the water resonance between −5 and 5 ppm, with a reference image at 300 ppm, and we systematically increased the B_1 pulse amplitude from 0.6 to 1.2 µT in 0.1 µT (in situ) or 0.3 µT (in vivo) steps. In addition, the pulse duration (t_p = 100 ms), pulse delay (t_d = 100 ms), and number of presaturation pulses (n_p = 40) were chosen to achieve a steady-state condition. For the B_0 inhomogeneity correction [51], a Water Saturation Shift Referencing (WASSR) sequence was acquired with t_p = 25 ms, t_d = 25 ms, n_p = 1, B_1 = 0.2 µT, 22 dynamics, and frequency

offsets between −1 and 1 ppm [52]; otherwise, the same sequence parameters were used for the CEST sequence.

Table 3. Magnetic resonance imaging sequence parameters.

	T1w TSE	T2w TSE *	T1 Mapping [A]	T2-SE Mapping	CEST In Situ [C]	CEST In Vivo [D]	WASSR
Orientation	sag	sag	sag	sag	sag	sag	sag
TE (ms)	9.8	95	10	[B]	3.5	3.5	3.5
TR (ms)	650	3500	6000	1000	2500	2500	2500
Slices	15	15	1	1	1	1	1
Slice Thickness (mm)	3	4	4	4	4	6	4/6
FOV (mm × mm)	300 × 300	260 × 260	200 × 200	200 × 200	200 × 200	200 × 200	200 × 200
Image matrix (pixel)	384 × 384	384 × 384	128 × 128	128 × 128	128 × 128	128 × 128	128 × 128
Flip angle (°)	150	160	180	180	15	15	15
Turbo Factor	109	17	11	na	na	na	na
GRAPPA	2	na	2	na	na	na	na
Duration (min:s)	1:12	3:46	8:38	1:12	84:35	36:15	3:43

*—only in vivo
[A]—TI = 25, 50, 100, 500, 1000, 2000 and 3000 ms
[B]—TE = 9.7 ms to 197 ms with a step size of 9.7 ms
[C]—B_1 = 0.6, 0.7, 0.8, 0.9, 1.0, 1.1, 1.2 µT; t_p = 100; t_d = 100 ms and n_p = 40
[D]—B_1 = 0.6, 0.9, 1.2 µT; t_p = 100 ms; t_d = 100 ms and n_p = 40

Abbreviations: T1w—T1 weighted; TSE—turbo spin echo; SE—spin echo; CEST—chemical exchange saturation transfer; WASSR—water saturation shift referencing; sag—sagittal; TE—echo time, TR—repetition time, FOV—field of view; na—not available; GRAPPA—Generalized Autocalibrating Partial Parallel Acquisition; TI—inversion time; B_1—high-frequency field strength; t_p—pulse duration; t_d—interpulse delay; n_p—number of saturation pulses.

4.3. In Silico Study

In accordance with previous studies, we simulated the Z-spectra based on the Bloch–McConnell equations using a house intern modified version of the open-source MATLAB (MatlabR2020b, Natick, MA, USA) script published by Zaiss et al. (Link to download: https://github.com/cest-sources/BM_sim_fit/, accessed on 16 March 2021) [13,19,53–55]. We evaluated the accuracy of the AREX- and LAREX-based Ω-plot analyses as a function of fractional GAG concentration f_b and hydroxyl proton exchange rate k_{ba}. Previously, Stabinska et al. showed that AREX-based Ω-plot analyses are varyingly accurate as a function of f_b and k_{ba} [17]. Therefore, we performed additional ideal simulations for a two-pool system consisting solely of water and the substrate to compare our multi-pool results. The same MR (TR = 2500 ms, TE = 3.5 ms) and presaturation parameters (n_p = 40, t_p = 100 ms, t_d = 100 ms, presaturation pulse shape = Gaussian, $\Delta\omega$ = 5 ppm) as well as a field strength of 3T were used for the simulations and the subsequent in situ and in vivo reference studies. GAG concentrations were systematically varied from 10 mM to 250 mM (f_b = 0.23–8.52‰) in an extended physiological range [19,31,56]. Accordingly, OH proton exchange rates k_{ba} were varied between 50 and 1000 Hz as described in previous studies [31,57]. A water concentration of 80% in IVDs was assumed, as shown by Baldoni et al. [29]; the other parameters used are listed with references in Table 1.

We also performed further in silico analyses, which can be found in Appendix A. In these analyses, we investigated our proposed LAREX-based Ω-plot approach for APT qCEST imaging in white matter (Appendix A Figure A1) and gray matter (Appendix A Figure A2), APT qCEST imaging of blood (Appendix A Figure A3), and creatine qCEST imaging in the human brain (Appendix A Figure A4) to illustrate its clinical applicability to a wide range of clinically relevant multi-pool systems.

4.4. In Situ Study

Human lumbar intervertebral disc cadavers: The local Institute of Anatomy I (Heinrich Heine University, Düsseldorf, Germany) provided eleven freshly frozen human IVDs

from three body donors for the in situ measurements. At the time of death, the mean age of the body donors was 88.6 ± 8.7 years (range 82–101 years), one was female, and two were male. Before each MRI examination, specimens were thawed and warmed to room temperature for at least 24 hours.

In situ MR imaging: All specimens were positioned centrally in the dedicated knee coil. In addition, mechanical positioning devices such as sandbags were used to fix the specimens in the coil. A baseline morphological T1w sequence was acquired to align the bio-sensitive imaging sequences. Subsequently, the specimens were examined with seven different B_1 field strengths as described above. Consistent with previous studies, a WASSR sequence was used for B_0 inhomogeneity correction [3,8,19].

Histological preparation: Following the MRI examination, the specimens were subjected to a standard histological procedure [58]. For this purpose, the IVDs and adjacent vertebrae were decalcified and fixed in Ossa fixona (Diagonal, Münster, Germany), dehydrated, and embedded in paraffin. IVDs were then cut along the mid-sagittal plane. The initial condition of the discs was semi-quantitatively scored according to Thompson et al. [29]. Thompson scoring. as the gold standard, allows for a full assessment of the degenerative stage of discs (score 1—no degeneration, score 5—fully degenerative IVD). T.J.F., who has 33 years of experience in musculoskeletal histopathology, assessed each tissue sample individually. In addition, IVDs were cut into 5-µm-thick slices and stained with Safranin O to validate the Thompson assessments [59]. A conventional light microscope (Motic Easy Scan Infinity 100, MoticEurope, Barcelona, Spain) and dedicated software (Motic® Images Devices MoticEurope, Barcelona, Spain) were used for validation; deviating staining compared to the Thompson score would lead to IVD exclusion.

4.5. In Vivo Study

The in vivo study was carried out on eight volunteers (mean age: 29 ± 4 years; age range: 24 to 35 years; six male, two female) with various stages of disc degenerations. All subjects were positioned headfirst and supine in the center of the MRI scanner. Morphological sequences (i.e., T1w- and T2w-sequences) were obtained for clinical assessment, such as Pfirrmann scoring of IVDs [30]. To determine the Pfirrmann degree of IVD degeneration, signal intensity on T2-weighted MR images was used to estimate water content with morphologic parameters on a scale of 1 (no degeneration) to 5 (completely degenerated). To reduce scanning time, only three of the CEST sequences used for the in vivo experiments (B_1 = 0.6, 0.9, and 1.2 µT, t_p = 100 ms, n_p = 40, pulse shape = Gauss) were acquired. For the B_0 inhomogeneity correction, a WASSR sequence was performed according to the in situ measurements as previously described.

4.6. LAREX: Lorentzian-Corrected Apparent Exchange-Dependent Relaxation

The Lorentzian-corrected apparent exchange-dependent relaxation Ω-analysis is an extension of the classical AREX approach for systems with multiple pools, using Lorentzian analyses to eliminate the influence of other proton pools (Figure 5). Analogous to the AREX approach, Z-spectra were first normalized. Subsequently, the different overlapping proton pools affecting the CEST effect are fitted and corrected by Lorentzian analyses (Figure 5). Analogous to the AREX approach, Z-spectra were first normalized (step 1). Next, the different overlapping proton pools affecting the CEST effect are fitted by Lorentzian analyses (step 2, Figure 5A). Subsequently, 2-pool Z-spectra were calculated, which are composed of a superposition of the calculated water pool and the investigated metabolite pool, and MTR_{asym} curves were calculated (step 3, Figure 5B). Finally, the Z-spectra were evaluated analogously to the classical AREX approach, where the measured Z-spectra were replaced by the corrected Z-spectra (step 4, Figure 5C). Therefore, for the IVDs experiments, the Z spectra were fitted considering the nuclear Overhauser enhancement—NOE #1 (−1.6 ppm), NOE #2 (−3.5 ppm), MT, spillover, OH, and NH effects. Due to the large number of free hyperparameters that arise in a multi-pool system, we used a user-defined error function (Equation (1)). For curve fitting, we used the MATLAB optimization solver

fmincon (find minimum of constrained nonlinear multivariable function) with a state-of-the-art sequential quadratic (SQP) algorithm. [60]. Following this correction mechanism, the Z-spectrum corresponds only to a two-pool system, which can be evaluated analogously to previous studies using AREX [17,22].

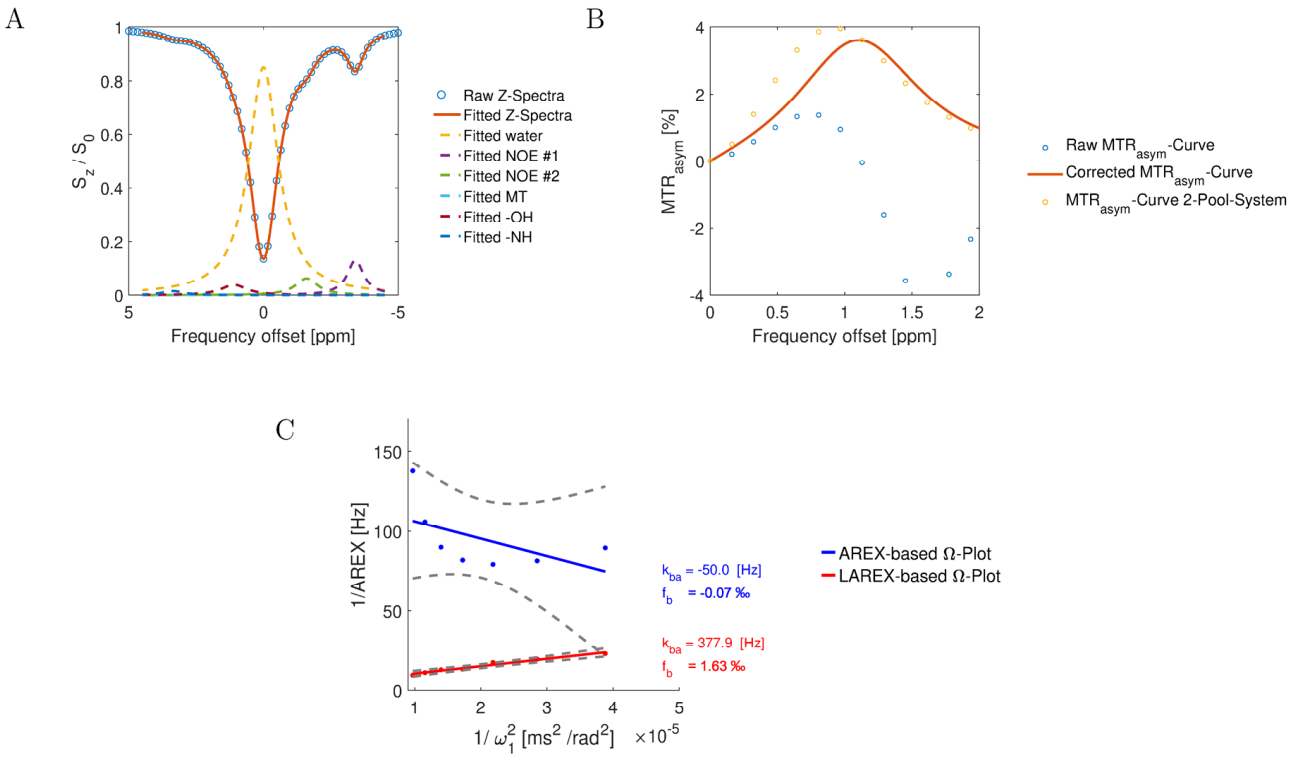

Figure 5. Graphical representation of an Ω-plot analysis using AREX and LAREX data, with Bloch–McConnell simulated Z-spectra for a 6-pool IVD exchange system. For the analysis, the parameters of the hydroxyl pool were f_b = 1.8‰ and k_{ba} = 400 Hz. The other pools' parameters are outlined in Table 3. (**A**) Plot of an exemplary Z-spectra (blue circles) at B1 = 0.7 µT and the fitted Z-spectra (red line), and the Lorentz fits of each pool (colored dashed lines). (**B**) The plot of the MTR_{asym} curve for the simulated raw Z-spectra (blue circles, Raw MTR_{asym}-Curve), the MTR_{asym}-Curves based on the Lorentz corrected Z-spectra to a two-pool system of water and Gag-OH (red line, Corrected MTR_{asym}-Curve), and the ground truth MTR_{asym}-Curve with based on a Bloch–McConnell simulation with only 2-pools (yellow circles, MTR_{asym}-Curve 2-Pool-System). (**C**) Visualization of the AREX (blue line) or LAREX-based (red line) Ω-plots. The gray dashed lines illustrate the 95% confidence interval of the linear omega plots.

The error function we proposed is based on the arctangent, which had proven itself as an error function under the minimization of numerous hyperparameters in machine learning [61].

$$error\left(\vec{X}\right) = \left(arctan\left(mean\left(y - f_{Lorentzian}\left(\vec{X}\right)\right)\right)\right)^2 \quad (1)$$

where y corresponds to the simulated or measured values of the Z-spectra, $f_{Lorentzian}$ corresponds to the Lorentzian function, and $\vec{X}$ corresponds to the hyperparameters to be optimized. Compared to the commonly used Root-Mean-Squared-Error, the error function differs by an adaptive gradient around zero (Appendix B Figure A5). Since the Z-spectra are normalized to y-values between 0 and 1, just the range smaller than 1 is decisive for the behavior of the error functions. Table 4 shows the fitting parameters we used. For the Lorentzian analysis of the Z spectrum, the different pools are not fitted to a fixed frequency offset. Instead, they are determined in a frequency range (Table 4); these deviations from the presumed frequency offset were corrected where necessary by replacing the frequency

in the Lorentzian function with the assumed frequency. Consequently, no deviations from the assumed and evaluated frequency offsets are present in the corrected Z spectra of the LAREX evaluation. The subsequent calculations of the MTR_{Rex} maps, AREX maps, and Ω-plots were consistently performed.

Table 4. Starting points and boundaries of the amplitude (A), width (W), and offset (Δ) of the six-pool Lorentzian fit, which we used for our in silico, in situ, and in vivo studies of IVDs. Furthermore, we used a custom loss function (Equation (1)).

	A_{water}	W_{water}	Δ_{water}	A_{amide}	W_{amide}	Δ_{amide}	$A_{hydroxyl}$	$W_{hydroxyl}$	$\Delta_{hydroxyl}$
Start	0.85	2	0	0.01	1	3.5	0.01	1	1
Lower	0.5	1	−0.5	0	0.2	3	0	0.5	0.6
Upper	1.1	6	0.5	0.1	3	4	0.1	2	1.4
	$A_{NOE\ \#1}$	$W_{NOE\ \#1}$	$\Delta_{NOE\ \#1}$	$A_{NOE\ \#2}$	$W_{NOE\ \#2}$	$\Delta_{NOE\ \#2}$	A_{MT}	W_{MT}	Δ_{MT}
Start	0.001	1	−1.6	0.03	1	−3.5	0.1	10	−2.3
Lower	0	0.5	−2.5	0	0.5	−5	0	8	−3
Upper	0.1	3.5	−0.5	0.2	4	−3	0.5	20	−2

4.7. MR Image Analysis

For further data analysis, the acquired in situ and in vivo MR data were segmented independently by two experienced radiologists, L.M.W. (5 years of musculoskeletal imaging experience) and D.B.A. (6 years of musculoskeletal imaging experience), using ITK Snap software (v3.8.0, Cognitica, Philadelphia, PA, USA) [62]. L.M.W. segmented the ROIs twice (i.e., six weeks apart) to assess the intra-reader reliability of the techniques studied, whereas D.B.A. segmented the data only once to determine inter-reader reliability. In addition, D.B.A. assessed the Pfirrmann grade for the in vivo measurements [30]. Additionally, tissue properties were further analyzed using in-house developed MATLAB scripts. T_1 maps were created by fitting the IR measurement data with the non-linear least-squares method as a function of inversion delay (TI): $S(TI) \sim S_0\ (1 - 2 \times \exp(-TI/T1))$, where S_0 is the equilibrium signal. T_2 maps were consistently calculated pixel-wise as a function of echo time (TE): $S(TE) \sim S_0 \times \exp(-TE/T2)$. Based on the WASSR measurements, the pixel-wise B_1 inhomogeneity offset maps were calculated. The CEST data were normalized to the signal of the first acquired frame with a frequency offset of 300 ppm. Using a custom MATLAB script validated in previous in silico and in vitro studies, the subsequent Ω-plots were performed [17]. To this end, the MR images were first denoised using the non-local means (NLM) filter [48], and Z-spectra were frequency corrected using the offset maps; the MTR_{Rex} maps with inverse asymmetry; and the AREX maps determined with the frequency shift of 1 ppm specific to hydroxyl protons. Subsequently, the relaxation-compensated Ω-plot analysis was calculated. In addition, an R_{2b} of 100 Hz was assumed for the hydroxyl protons bounded on GAG in accordance with Singh et al. [28].

4.8. Statistical Analysis

Statistical analyses were made by K.L.R. in R (v4.1.3, R Foundation for Statistical Computing). The Kendall-Tau rank correlation coefficient (τ) was determined to investigate possible statistical relationships between the determined surrogate parameters f_b and k_{ba} as a function of the histological Thompson classification (in situ) and Pfirrmann scoring (in vivo). The tau effect size was classified as low (0.1–0.3), medium (0.3–0.5), and strong (>0.5), according to Cohen et al. [63]. To measure relative reliability, the intraclass correlation coefficient (ICC) was used with a 95% confidence interval and was classified according to Koo et al. as poor ($ICC < 0.5$), moderate ($0.5 \leq ICC < 0.75$), good ($0.75 \leq ICC < 0.9$), and excellent ($ICC \geq 0.9$) [64]. For determining inter-rater reliability, the ICC(2,1) was used, and intra-rater reliability was determined using the ICC(3,1) [65].

Due to the experimental design of this study, the significance level was set from $p \leq 0.05$ to an adjusted $p \leq 0.00625$ according to the conservative alpha adjustment method

Bonferroni [66]. This "low" significance level prevented alpha error inflation while simultaneously maintaining statistical power.

5. Conclusions

In our study of qCEST imaging in multi-pool models, we validated our proposed LAREX method using in silico experiments for a wide range of medically relevant systems such as human IVDs, the white and gray matter of the visual cortex, and human ex-vivo blood. Moreover, we have therefore shown that Lorentz analyses can be used to extract 2-pool spectra from multi-pool spectra. These calculated 2-pool spectra yield results comparable to real 2-pool spectra in an omega plot analysis. Furthermore, we could transfer the results to in situ and in vivo studies. Therefore, for the first time, it is possible to quantitatively investigate multi-pool systems by means of fractional concentration and exchange rate and by using qCEST with the LAREX approach.

Author Contributions: Conceptualization, K.L.R., L.M.W., M.F. and D.B.A.; methodology, K.L.R., J.S. and M.K.; software, K.L.R., J.S. and A.M.-L.; validation, K.L.R. and M.K.; formal analysis, K.L.R., M.K. and T.J.F.; investigation, K.L.R., M.F., M.K and B.K.; resources, T.J.F. and G.A.; data curation, K.L.R., M.F. and M.K.; writing—original draft preparation, K.L.R., L.M.W., D.B.A., H.-J.W. and A.M.-L.; writing—review and editing, K.L.R., L.M.W., M.F., J.S., M.K., B.K., T.A.T., T.J.F., S.N., G.A., D.B.A., H.-J.W. and A.M.-L.; visualization, K.L.R., L.M.W., T.A.T., H.-J.W. and A.M.-L.; supervision, K.L.R., L.M.W. and M.F.; project administration, K.L.R., L.M.W., M.F., B.K., S.N. and A.M.-L. All authors have read and agreed to the published version of the manuscript.

Funding: D.B.A., L.M.W., M.F. and S.N. were supported by grants from the local Research Committee of the Medical Faculty of Heinrich-Heine-University Düsseldorf, Germany. S.N. was additionally supported by "Deutsche Forschungsgemeinschaft" (DFG) (NE 2136/3-1).

Institutional Review Board Statement: The study was conducted according to the guidelines of the Declaration of Helsinki and approved by the Institutional Ethics Committee of Heinrich-Heine-University of Düsseldorf (protocol code 2021-1528 and 2019-551).

Informed Consent Statement: Informed consent was obtained from all subjects involved in the study.

Data Availability Statement: Data and evaluation scripts can be provided by the authors upon reasonable request.

Acknowledgments: We would like to express our sincere thanks for the excellent cooperation with the Institute of Anatomy I. Sabine Wittschonnke and Marco Warten are to be thanked, who prepared the IVDs for the MR examinations.

Conflicts of Interest: The authors declare no conflict of interest.

Appendix A

The following figures demonstrate the results for the transferability of our presented LAREX-based Ω-plot approach for other medically relevant multipool systems outside of human IVDs. The simulation parameters used for the longitudinal relaxation time (T_1), transverse relaxation time (T_2), fractional substrate concentration (f), and substrate exchange rate with the water pool (k_{ba}) are given for each pool in the corresponding figure captions below.

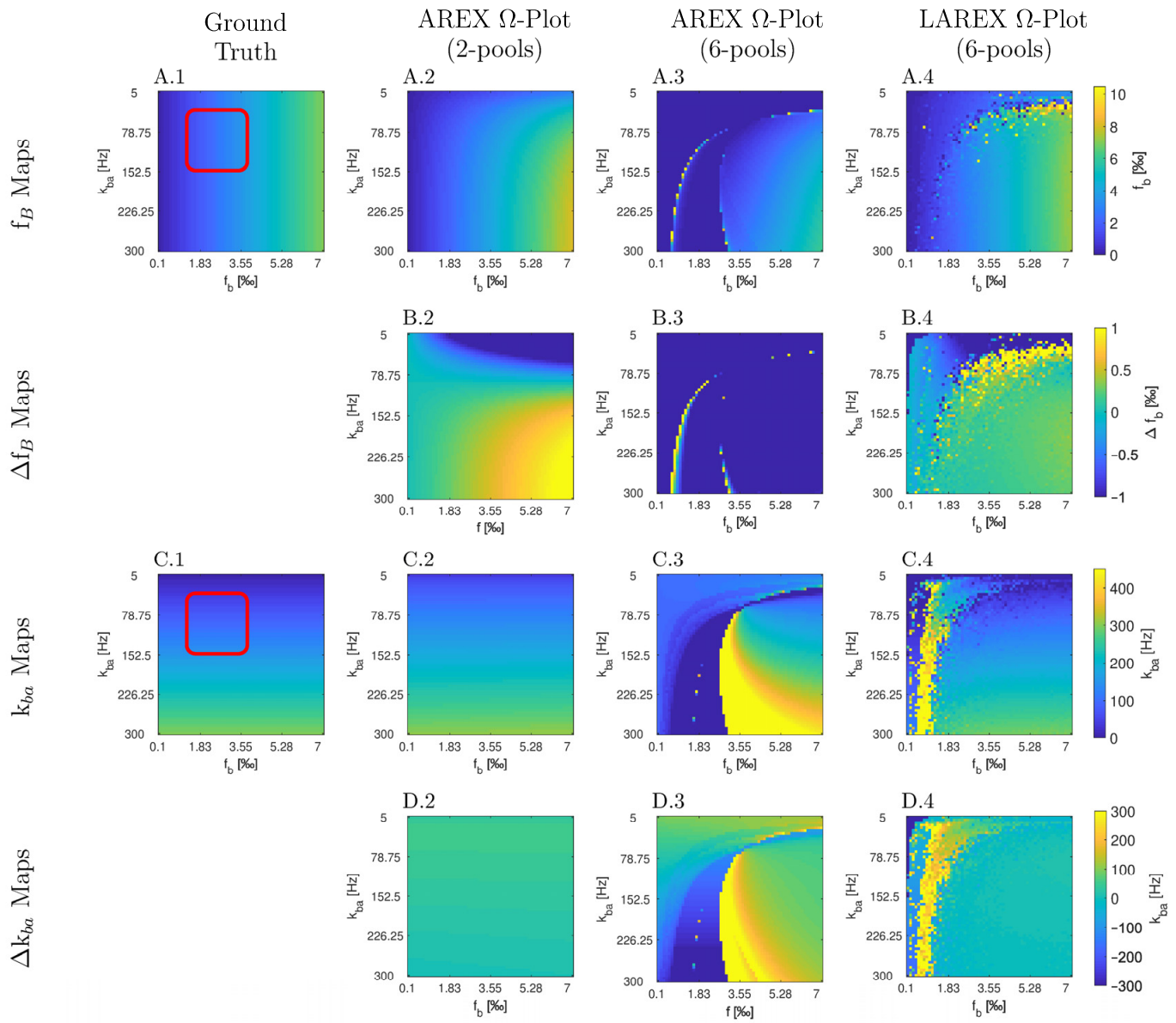

Figure A1. In silico Appendix Study 1—APT qCEST analyses of white matter of the visual cortex. Parameter maps (**A**,**C**) and color-coded error maps (**B**,**D**) for fractional APT concentrations f_b and exchange rates k_{ba} as a function of f_b and k_{ba}. The study was performed using a 4-pool system and a field strength of 7 Tesla. The parameters of the exchanging proton pools were: Water (T_1 = 1200 ms, T_2 = 40 ms, and Δ = 0 ppm); APT (T_1 = 1000 ms, T_2 = 10 ms, f = variable between 0.001–0.2, k_{ba} = variable between 1–300 Hz, and Δ = 3.5); NOE (T_1 = 1000 ms, T_2 = 0.3 ms, f_s = 0.06, k_{ba} = 10 Hz, and Δ_s = −3.5 ppm); MT (T_1 = 1000 ms, T_2 = 10 µs, f_s = 0.11, k_{ba} = 50 Hz, and Δ_s = 0 ppm), and were based on the results of Mougin et al. [67]. Furthermore, analogous to the in silico, in situ, and in vivo experiments, the same MR parameters (TR = 2500 ms, TE = 3.5 ms) and presaturation parameters (n_p = 40, t_p = 100 ms, t_d = 100 ms, presaturation pulse shape = Gaussian, Δω = 5 ppm) were used.

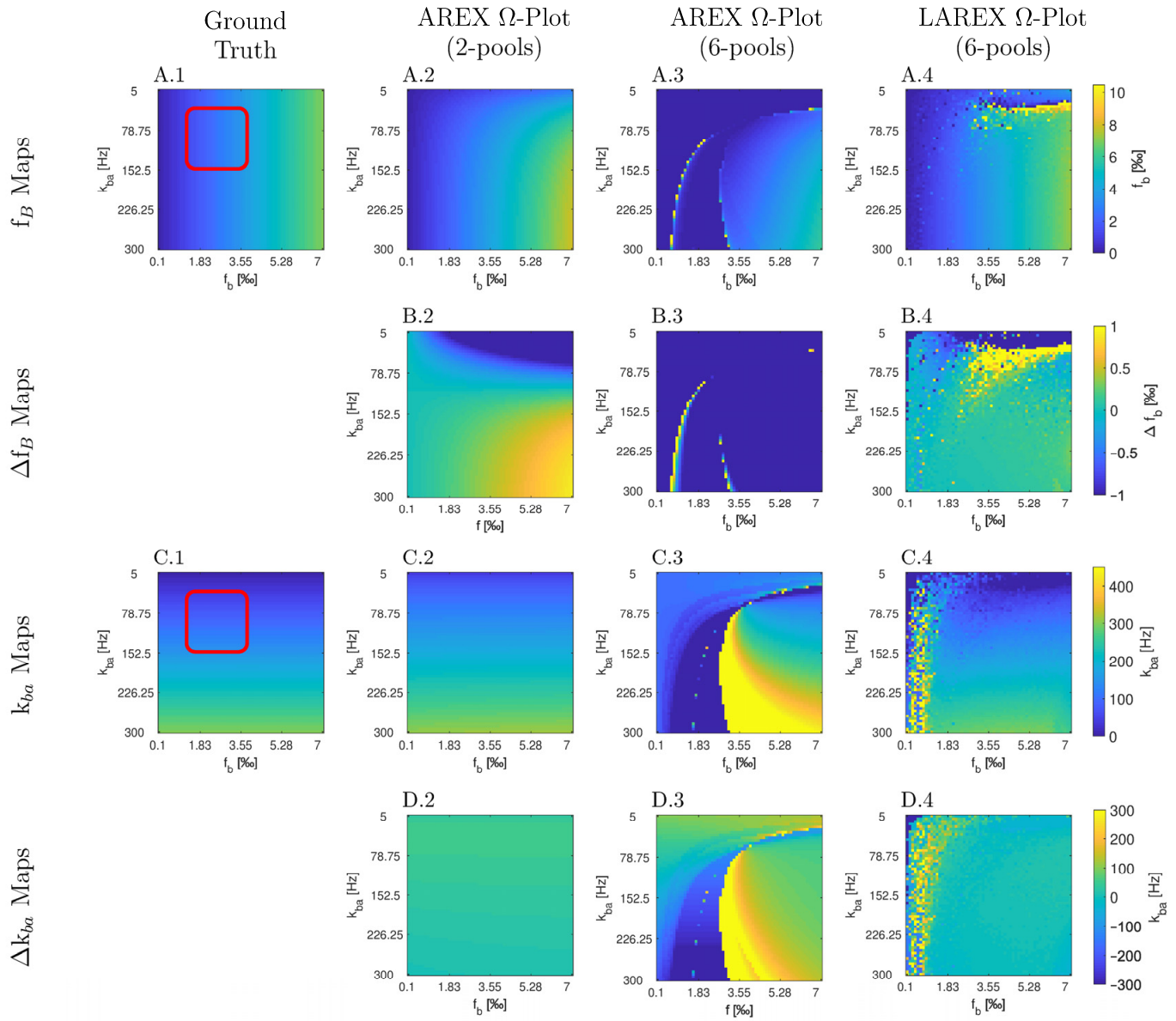

Figure A2. In silico Appendix Study 2—APT qCEST analyses of gray matter of the visual cortex. Parameter maps (**A**,**C**) and color-coded error maps (**B**,**D**) for fractional APT concentrations f_b and exchange rates k_{ba} as a function of f_b and k_{ba}. The study was performed using a 4-pool system and a field strength of 7 Tesla. The parameters of the exchanging proton pools were: Water (T_1 = 2000 ms, T_2 = 55 ms, and Δ = 0 ppm); APT (T_1 = 1000 ms, T_2 = 10 ms, f = variable between 0.001–0.01, k_{ba} = variable between 0–300 Hz, and Δ = 3.5); NOE (T_1 = 1000 ms, T_2 = 0.3 ms, f = 0.06, k_{ba} = 10 Hz, and Δ_s = −3.5 ppm); MT (T_1 = 1000 ms, T_2 = 10 µs, f = 0.11, k_{ba} = 50 Hz, and Δ = 0 ppm), and were based on the results of Mougin et al. [67]. Furthermore, analogous to the in silico, in situ, and in vivo experiments, the same MR parameters (TR = 2500 ms, TE = 3.5 ms) and presaturation parameters (n_p = 40, t_p = 100 ms, t_d = 100 ms, presaturation pulse shape = Gaussian, Δω = 5 ppm) were used.

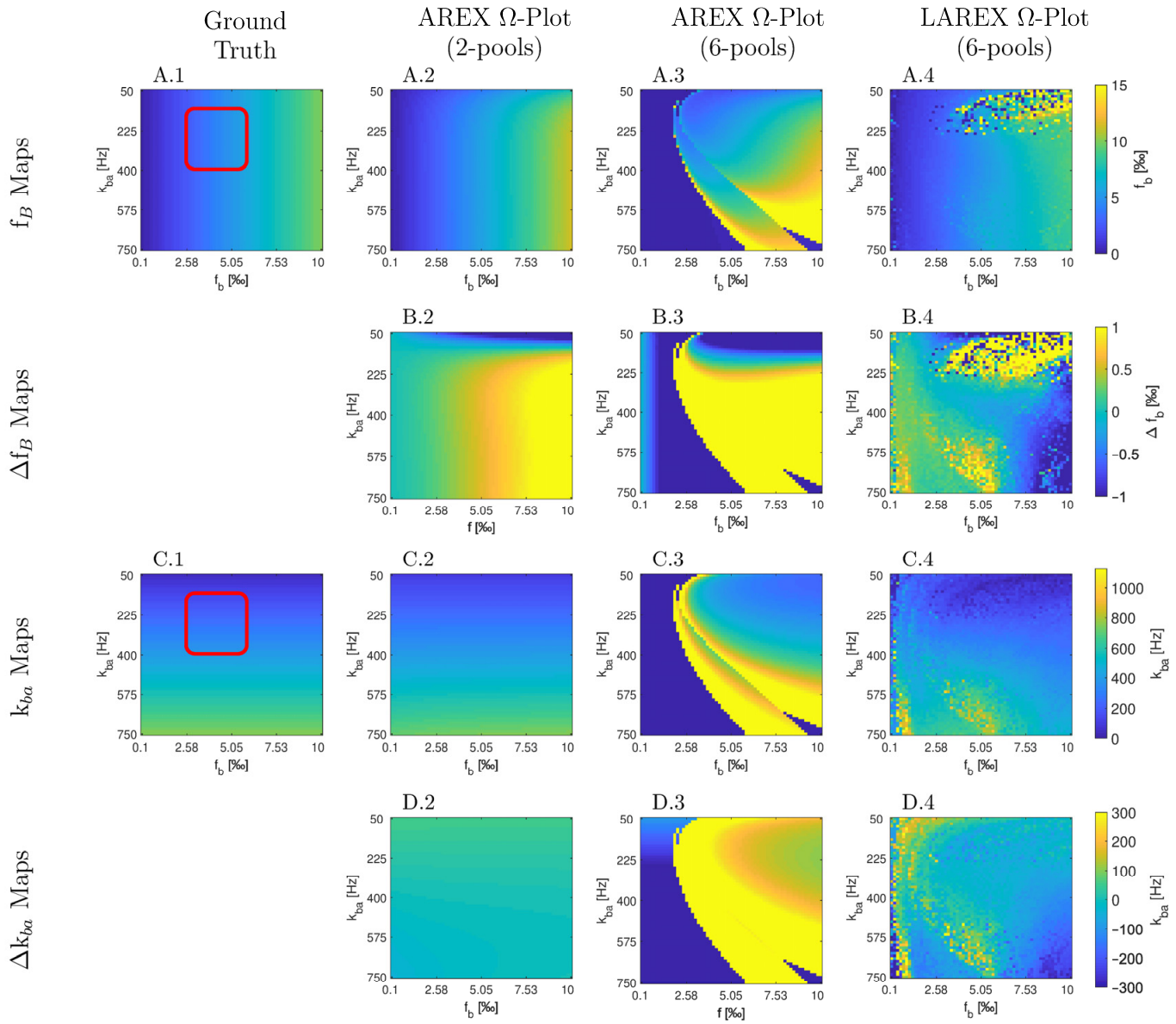

Figure A3. In silico Appendix Study 3—Amine qCEST analyses of the human ex-vivo blood. Parameter maps (**A**,**C**) and color-coded error maps (**B**,**D**) for fractional Amine concentrations f_b and APT exchange rates k_{ba} as a function of f_b and k_{ba}. The study was performed using a 6-pool system and a field strength of 7 Tesla. The parameters of the exchanging proton pools were: Water (T_1 = 2249 ms, T_2 = 48.5 ms, and Δ_s = 0 ppm); Amine (T_1 = 1000 ms, T_2 = 10 ms, f = variable 0.0001–0.01, k_{ba} = variable 50–750 Hz and Δ = 2.2); APT (T_1 = 1000 ms, T_2 = 0.5 ms, f = 0.0078, k_{ba} = 338.7 and Δ_s = 3.5); NOE #1 (T_1 = 1000 ms, T_2 = 1.2 ms, f = 0.018, k_{ba} = 10 Hz and Δ = −1.7 ppm); NOE #2 (T_1 = 1000 ms, T_2 = 0.5 ms, f = 0.0144, k_{ba} = 5 Hz and Δ_s = −3.5); MT (T_1 = 1000 ms, T_2 = 0.01 ms, f = 0.0105, k_{ba} = 15 and Δ = −2.34), and were based on the results of Shah et al. [68]. Furthermore, analogous to the in silico, in situ, and in vivo experiments, the same MR parameters (TR = 2500 ms, TE = 3.5 ms) and presaturation parameters (n_p = 40, t_p = 100 ms, t_d = 100 ms, presaturation pulse shape = Gaussian, $\Delta\omega$ = 5 ppm) were used.

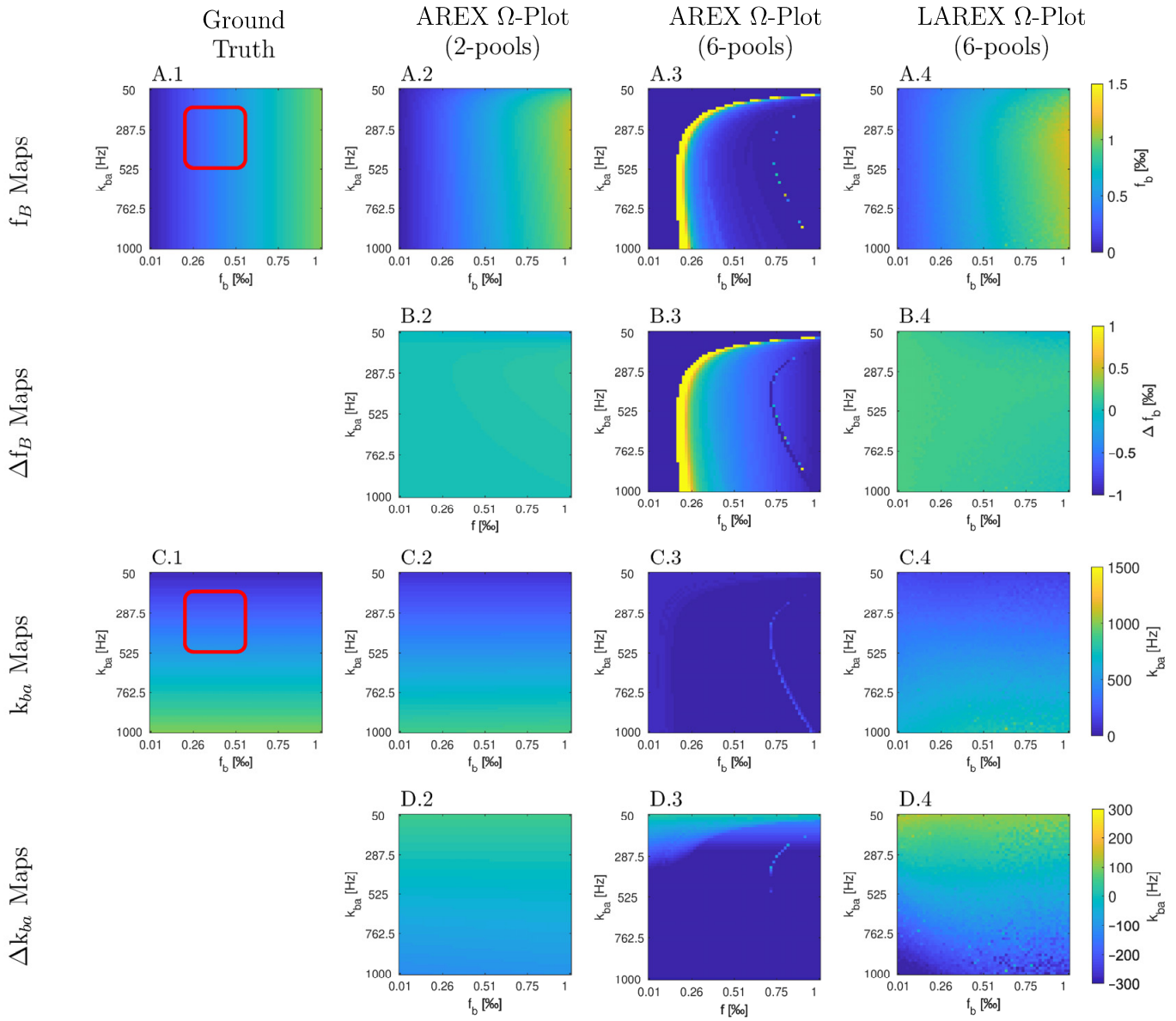

Figure A4. In silico Appendix Study 4—Creatine qCEST analyses of human brain. Parameter maps (**A**,**C**) and color-coded error maps (**B**,**D**) for fractional Creatine concentrations f_b and Creatine exchange rates k_{ba} as a function of f_b and k_{ba}. The study was performed using a 6-pool system and a field strength of 7 Tesla. The parameters of the exchanging proton pools were: Water (T_1 = 2000 ms, T_2 = 115 ms, and Δ = 0 ppm); Creatine (T_1 = 1000 ms, T_2 = 10 ms, f = variable 0.00001–0.001, k_{sw} = variable 50–1000 Hz and Δ = 1.8); Amide (T_1 = 1000 ms, T_2 = 33 ms, f = 0.0008, k_{ba} = 30 and Δ = 3.5); Glutamate (T_1 = 1000 ms, T_2 = 10 ms, f_s = 0.000125, k_{sw} = 2000 and $Δ_s$ = 3.0); Myo-inositol (T_1 = 1000 ms, T_2 = 10 ms, f = 0.0007, k_{ba} = 600 and Δ = 0.6); NOE (T_1 = 1000 ms, T_2 = 0.01 ms, f = 0.0795, k_{ba} = 10 and Δ = −2.4), and were based on the results of Sing et al. [69]. Furthermore, analogous to the in silico, in situ, and in vivo experiments, the same MR parameters (TR = 2500 ms, TE = 3.5 ms) and presaturation parameters (n_p = 40, t_p = 100 ms, t_d = 100 ms, presaturation pulse shape = Gaussian, Δω = 5 ppm) were used.

Appendix B

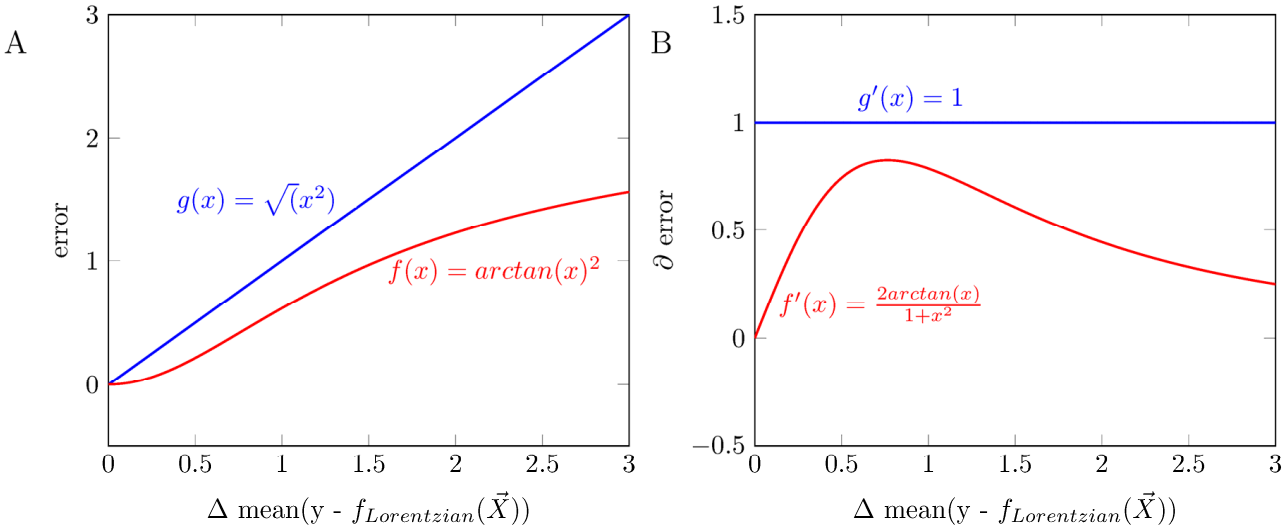

Figure A5. Comparison of arctan as an error function versus the commonly used Root Mean Squared Error (RMSE) function. (**A**) Calculated error as a function of the mean deviation. (**B**) The course of the gradient of the error function as a function of the mean deviation. Here, the arctan shows an adaptive adjustment of the error gradient, which is especially advantageous for optimizing many hyperparameters.

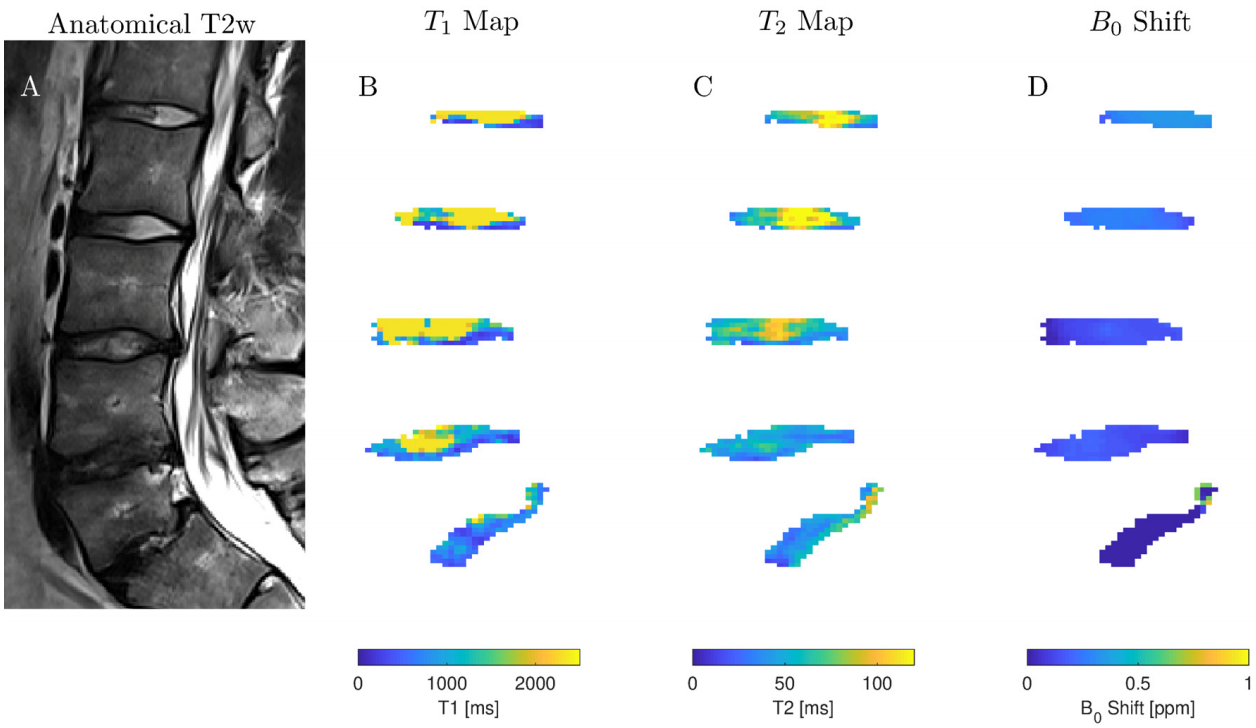

Figure A6. A sagittal T2-weighted (T2w) image (**A**) of the volunteer shown in Figure 4 and the corresponding longitudinal relaxation time (T1) map (**B**), transverse relaxation time (T2) map (**C**), and B0 field displacement map (**D**).

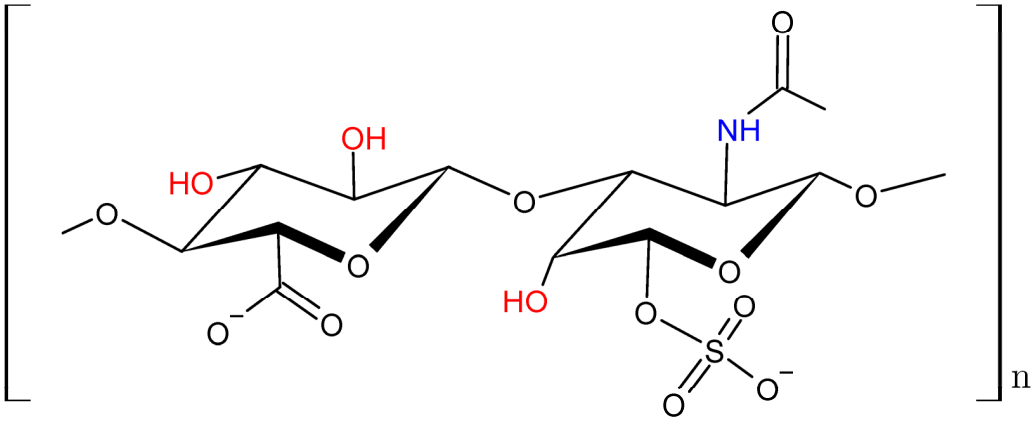

Figure A7. The molecular formula of chondroitin sulfate, the most abundant glycosaminoglycan in cartilage. The three exchanging hydroxyl groups (-OH) are highlighted in red, and the one exchanging amide group (-NH) in blue.

References

1. Fatoye, F.; Gebrye, T.; Odeyemi, I. Real-world incidence and prevalence of low back pain using routinely collected data. *Rheumatol. Int.* **2019**, *39*, 619–626. [CrossRef] [PubMed]
2. Suthar, P.; Patel, R.; Mehta, C.; Patel, N. Mri Evaluation of Lumbar Disc Degenerative Disease. *J. Clin. Diagn. Res. JCDR* **2015**, *9*, Tc04–Tc09. [CrossRef] [PubMed]
3. Frenken, M.; Nebelung, S.; Schleich, C.; Müller-Lutz, A.; Radke, K.; Kamp, B.; Boschheidgen, M.; Wollschläger, L.; Bittersohl, B.; Antoch, G.; et al. Non-Specific Low Back Pain and Lumbar Radiculopathy: Comparison of Morphologic and Compositional MRI as Assessed by gagCEST Imaging at 3T. *Diagnostics* **2021**, *11*, 402. [CrossRef] [PubMed]
4. Wollschläger, L.; Nebelung, S.; Schleich, C.; Müller-Lutz, A.; Radke, K.; Frenken, M.; Boschheidgen, M.; Prost, M.; Antoch, G.; Konieczny, M.; et al. Evaluating Lumbar Intervertebral Disc Degeneration on a Compositional Level Using Chemical Exchange Saturation Transfer: Preliminary Results in Patients with Adolescent Idiopathic Scoliosis. *Diagnostics* **2021**, *11*, 934. [CrossRef] [PubMed]
5. Kamp, B.; Frenken, M.; Henke, J.M.; Abrar, D.B.; Nagel, A.M.; Gast, L.V.; Oeltzschner, G.; Wilms, L.M.; Nebelung, S.; Antoch, G.; et al. Quantification of Sodium Relaxation Times and Concentrations As Surrogates of Proteo-glycan Content of Patellar Cartilage at 3t MRI. *Diagnostics* **2021**, *11*, 2301. [CrossRef] [PubMed]
6. Truhn, D.; Zwingenberger, K.T.; Schock, J.; Abrar, D.B.; Radke, K.L.; Post, M.; Linka, K.; Knobe, M.; Kuhl, C.; Nebelung, S. No Pressure, No Diamonds?—Static vs. Dynamic Compressive In-Situ Loading to Evaluate Human Articular Cartilage Functionality by Functional MRI. *J. Mech. Behav. Biomed. Mater.* **2021**, *120*, 104558. [CrossRef]
7. Thiel, T.A.; Schweitzer, J.; Xia, T.; Bechler, E.; Valentin, B.; Steuwe, A.; Boege, F.; Westenfeld, R.; Wittsack, H.-J.; Ljimani, A. Evaluation of Radiographic Contrast-Induced Nephropathy by Functional Diffusion Weighted Imaging. *J. Clin. Med.* **2021**, *10*, 4573. [CrossRef]
8. Müller-Lutz, A.; Ljimani, A.; Stabinska, J.; Zaiss, M.; Boos, J.; Wittsack, H.-J.; Schleich, C. Comparison of B0 versus B0 and B1 field inhomogeneity correction for glycosaminoglycan chemical exchange saturation transfer imaging. *Magn. Reson. Mater. Phys. Biol. Med.* **2018**, *31*, 645–651. [CrossRef]
9. Sasisekharan, R.; Raman, R.; Prabhakar, V. Glycomics Approach to Structure-Function Relationships of Glycosaminoglycans. *Annu. Rev. Biomed. Eng.* **2006**, *8*, 181–231. [CrossRef]
10. Ling, W.; Regatte, R.R.; Navon, G.; Jerschow, A. Assessment of glycosaminoglycan concentration in vivo by chemical exchange-dependent saturation transfer (gagCEST). *Proc. Natl. Acad. Sci. USA* **2008**, *105*, 2266–2270. [CrossRef]
11. Schiebler, T.H. (Ed.) *Anatomie: Zytologie, Histologie, Entwicklungsgeschichte, Makroskopische Und Mikroskopische Anatomie Des Menschen*; Unter Berücksichtigung Des Gegenstandskatalogs; Mit 119 Tabellen; Springer: Berlin/Heidelberg, Germany, 1999.
12. Ward, K.M.; Aletras, A.H.; Balaban, R.S. A New Class of Contrast Agents for MRI Based on Proton Chemical Exchange De-pendent Saturation Transfer (Cest). *J. Magn. Reson.* **2000**, *143*, 79–87. [CrossRef] [PubMed]
13. Radke, K.L.; Abrar, D.B.; Frenken, M.; Wilms, L.M.; Kamp, B.; Boschheidgen, M.; Liebig, P.; Ljimani, A.; Filler, T.J.; Antoch, G.; et al. Chemical Exchange Saturation Transfer for Lactate-Weighted Imaging at 3 T MRI: Comprehensive In Silico, In Vitro, In Situ, and In Vivo Evaluations. *Tomography* **2022**, *8*, 1277–1292. [CrossRef] [PubMed]
14. Sun, P.Z. Simplified and scalable numerical solution for describing multi-pool chemical exchange saturation transfer (CEST) MRI contrast. *J. Magn. Reson.* **2010**, *205*, 235–241. [CrossRef] [PubMed]
15. Sun, P.Z.; Wang, Y.; Xiao, G.; Wu, R. Simultaneous experimental determination of labile proton fraction ratio and exchange rate with irradiation radio frequency power-dependent quantitative CEST MRI analysis. *Contrast Media Mol. Imaging* **2013**, *8*, 246–251. [CrossRef] [PubMed]

16. Zhang, S.; Malloy, A.C.R.; Sherry, A.D. MRI Thermometry Based on PARACEST Agents. *J. Am. Chem. Soc.* **2005**, *127*, 17572–17573. [CrossRef]
17. Stabinska, J.; Cronenberg, T.; Wittsack, H.-J.; Lanzman, R.S.; Müller-Lutz, A. Quantitative pulsed CEST-MRI at a clinical 3T MRI system. *Magn. Reson. Mater. Phys. Biol. Med.* **2017**, *30*, 505–516. [CrossRef]
18. Vinogradov, E.; Sherry, D.; Lenkinski, R. CEST: From basic principles to applications, challenges and opportunities. *J. Magn. Reson.* **2012**, *229*, 155–172. [CrossRef]
19. Abrar, D.B.; Schleich, C.; Radke, K.L.; Frenken, M.; Stabinska, J.; Ljimani, A.; Wittsack, H.-J.; Antoch, G.; Bittersohl, B.; Hesper, T.; et al. Detection of early cartilage degeneration in the tibiotalar joint using 3 T gagCEST imaging: A feasibility study. *Magn. Reson. Mater. Phys. Biol. Med.* **2020**, *34*, 249–260. [CrossRef]
20. Dixon, W.T.; Ren, J.; Lubag, A.J.M.; Ratnakar, J.; Vinogradov, E.; Hancu, I.; Lenkinski, R.E.; Sherry, A.D. A Concentration-Independent Method to Measure Exchange Rates in Paracest Agents. *Magn. Reson. Med.* **2010**, *63*, 625–632. [CrossRef]
21. Meissner, J.-E.; Goerke, S.; Rerich, E.; Klika, K.D.; Radbruch, A.; Ladd, M.E.; Bachert, P.; Zaiss, M. Quantitative pulsed CEST-MRI using Ω-plots. *NMR Biomed.* **2015**, *28*, 1196–1208. [CrossRef]
22. Sun, P.Z.; Wang, Y.; Dai, Z.; Xiao, G.; Wu, R. Quantitative chemical exchange saturation transfer (qCEST) MRI-RF spillover effect-corrected omega plot for simultaneous determination of labile proton fraction ratio and exchange rate. *Contrast Media Mol. Imaging* **2014**, *9*, 268–275. [CrossRef] [PubMed]
23. Zaiss, M.; Xu, J.; Goerke, S.; Khan, I.S.; Singer, R.J.; Gore, J.C.; Gochberg, D.F.; Bachert, P. Inverse Z-Spectrum Analysis for Spillover-, Mt-, and T1 -Corrected Steady-State Pulsed Cest-MRI—Application to Ph-Weighted MRI of Acute Stroke. *NMR Biomed.* **2014**, *27*, 240–252. [CrossRef]
24. Warnert, E.A.H.; Wood, T.C.; Incekara, F.; Barker, G.J.; Vincent, A.J.P.; Schouten, J.; Kros, J.M.; Bent, M.V.D.; Smits, M.; Tamames, J.A.H. Mapping tumour heterogeneity with pulsed 3D CEST MRI in non-enhancing glioma at 3 T. *Magn. Reson. Mater. Phys. Biol. Med.* **2021**, *35*, 53–62. [CrossRef] [PubMed]
25. Zhang, X.-Y.; Wang, F.; Li, H.; Xu, J.; Gochberg, D.F.; Gore, J.C.; Zu, Z. Accuracy in the quantification of chemical exchange saturation transfer (CEST) and relayed nuclear Overhauser enhancement (rNOE) saturation transfer effects. *NMR Biomed.* **2017**, *30*, e3716. [CrossRef] [PubMed]
26. Schüre, J.; Shrestha, M.; Breuer, S.; Deichmann, R.; Hattingen, E.; Wagner, M.; Pilatus, U. The pH sensitivity of APT-CEST using phosphorus spectroscopy as a reference method. *NMR Biomed.* **2019**, *32*, e4125. [CrossRef]
27. Zaiß, M.; Schmitt, B.; Bachert, P. Quantitative separation of CEST effect from magnetization transfer and spillover effects by Lorentzian-line-fit analysis of z-spectra. *J. Magn. Reson.* **2011**, *211*, 149–155. [CrossRef]
28. Singh, A.; Haris, M.; Cai, K.; Kassey, V.B.; Kogan, F.; Reddy, D.; Hariharan, H.; Reddy, R. Chemical exchange saturation transfer magnetic resonance imaging of human knee cartilage at 3 T and 7 T. *Magn. Reson. Med.* **2011**, *68*, 588–594. [CrossRef]
29. Thompson, J.P.; Pearce, R.H.; Schechter, M.T.; Adams, M.E.; Tsang, I.K.Y.; Bishop, P.B. Preliminary Evaluation of a Scheme for Grading the Gross Morphology of the Human Intervertebral Disc. *Spine* **1990**, *15*, 411–415. [CrossRef]
30. Pfirrmann, C.; Metzdorf, A.; Zanetti, M.; Hodler, J.; Boos, N. Magnetic Resonance Classification of Lumbar Intervertebral Disc Degeneration. *Spine* **2001**, *26*, 1873–1878. [CrossRef]
31. Zhou, Z.; Bez, M.; Tawackoli, W.; Giaconi, J.; Sheyn, D.; De Mel, S.; Maya, M.M.; Pressman, B.D.; Gazit, Z.; Pelled, G.; et al. Quantitative chemical exchange saturation transfer MRI of intervertebral disc in a porcine model. *Magn. Reson. Med.* **2016**, *76*, 1677–1683. [CrossRef]
32. Müller-Lutz, A.; Schleich, C.; Pentang, G.; Schmitt, B.; Lanzman, R.S.; Matuschke, F.; Wittsack, H.-J.; Miese, F. Age-dependency of glycosaminoglycan content in lumbar discs: A 3t gagcEST study. *J. Magn. Reson. Imaging* **2015**, *42*, 1517–1523. [CrossRef] [PubMed]
33. Kauppinen, J.K.; Moffatt, D.J.; Mantsch, H.H.; Cameron, D.G. Smoothing of spectral data in the Fourier domain. *Appl. Opt.* **1982**, *21*, 1866–1872. [CrossRef] [PubMed]
34. Iatridis, J.C.; MacLean, J.J.; O'Brien, M.; Stokes, I. Measurements of Proteoglycan and Water Content Distribution in Human Lumbar Intervertebral Discs. *Spine* **2007**, *32*, 1493–1497. [CrossRef] [PubMed]
35. Roughley, F.J. The structure and function of cartilage proteoglycans. *Eur. Cells Mater.* **2006**, *12*, 92–101. [CrossRef]
36. Radke, K.; Wollschläger, L.; Nebelung, S.; Abrar, D.; Schleich, C.; Boschheidgen, M.; Frenken, M.; Schock, J.; Klee, D.; Frahm, J.; et al. Deep Learning-Based Post-Processing of Real-Time MRI to Assess and Quantify Dynamic Wrist Movement in Health and Disease. *Diagnostics* **2021**, *11*, 1077. [CrossRef]
37. Schock, J.; Truhn, D.; Nürnberger, D.; Conrad, S.; Huppertz, M.S.; Keil, S.; Kuhl, C.; Merhof, D.; Nebelung, S. Artificial Intel-ligence-Based Automatic Assessment of Lower Limb Torsion on MRI. *Sci. Rep.* **2021**, *11*, 23244. [CrossRef]
38. Müller-Franzes, G.; Nolte, T.; Ciba, M.; Schock, J.; Khader, F.; Prescher, A.; Wilms, L.M.; Kuhl, C.; Nebelung, S.; Truhn, D. Fast, Accurate, and Robust T2 Mapping of Articular Cartilage by Neural Networks. *Diagnostics* **2022**, *12*, 688. [CrossRef]
39. Zaiss, M.; Deshmane, A.; Schuppert, M.; Herz, K.; Glang, F.; Ehses, P.; Lindig, T.; Bender, B.; Ernemann, U.; Scheffler, K. DeepCEST: 9.4 T Chemical exchange saturation transfer MRI contrast predicted from 3 T data—A proof of concept study. *Magn. Reson. Med.* **2019**, *81*, 3901–3914. [CrossRef]
40. Huang, J.; Lai, J.H.C.; Tse, K.; Cheng, G.W.Y.; Liu, Y.; Chen, Z.; Han, X.; Chen, L.; Xu, J.; Chan, K.W.Y. Deep neural network based CEST and AREX processing: Application in imaging a model of Alzheimer's disease at 3 T. *Magn. Reson. Med.* **2021**, *87*, 1529–1545. [CrossRef]

41. Wei, W.; Jia, G.; Flanigan, D.; Zhou, J.; Knopp, M.V. Chemical exchange saturation transfer MR imaging of articular cartilage glycosaminoglycans at 3T: Accuracy of B0 Field Inhomogeneity corrections with gradient echo method. *Magn. Reson. Imaging* **2013**, *32*, 41–47. [CrossRef]
42. Liu, D.; Zhou, J.; Xue, R.; Wang, D.J.J. Using simultaneous multi-slice excitation to accelerate CEST imaging. In Proceedings of the 22nd Annual Meeting of ISMRM, Milan, Italy, 10–16 May 2014; p. 3294.
43. Randtke, E.A.; Granados, J.; Howison, C.M.; Pagel, M.D.; Cárdenas-Rodríguez, J. Multislice CEST MRI improves the spatial assessment of tumor pH. *Magn. Reson. Med.* **2016**, *78*, 97–106. [CrossRef] [PubMed]
44. Boutin, C.; Léonce, E.; Brotin, T.; Jerschow, A.; Berthault, P. Ultrafast Z-Spectroscopy for ^{129}Xe NMR-Based Sensors. *J. Phys. Chem. Lett.* **2013**, *4*, 4172–4176. [CrossRef] [PubMed]
45. Heo, H.; Zhang, Y.; Lee, D.-H.; Jiang, S.; Zhao, X.; Zhou, J. Accelerating chemical exchange saturation transfer (CEST) MRI by combining compressed sensing and sensitivity encoding techniques. *Magn. Reson. Med.* **2016**, *77*, 779–786. [CrossRef] [PubMed]
46. Zhang, Y.; Zu, T.; Liu, R.; Zhou, J. Acquisition sequences and reconstruction methods for fast chemical exchange saturation transfer imaging. *NMR Biomed.* **2022**, e4699. [CrossRef]
47. Zaiss, M.; Bachert, P. Chemical Exchange Saturation Transfer (Cest) and Mr Z-Spectroscopy In Vivo: A Review of Theoretical Approaches and Methods. *Phys. Med. Biol.* **2013**, *58*, R221–R269. [CrossRef]
48. Buades, A.; Coll, B.; Morel, J.-M. A non-local algorithm for image denoising. In Proceedings of the 2005 IEEE Computer Society Conference on Computer Vision and Pattern Recognition (Cvpr'05)—Workshops, San Diego, CA, USA, 20–25 June 2005; pp. 60–65.
49. Kubaski, F.; Osago, H.; Mason, R.W.; Yamaguchi, S.; Kobayashi, H.; Tsuchiya, M.; Orii, T.; Tomatsu, S. Glycosaminoglycans detection methods: Applications of mass spectrometry. *Mol. Genet. Metab.* **2016**, *120*, 67–77. [CrossRef]
50. Stover, J.D.; Lawrence, B.; Bowles, R.D. Degenerative IVD conditioned media and acidic pH sensitize sensory neurons to cyclic tensile strain. *J. Orthop. Res.* **2020**, *39*, 1192–1203. [CrossRef]
51. Kim, M.; Gillen, J.; Landman, B.A.; Zhou, J.; Van Zijl, P.C.M. Water Saturation Shift Referencing (Wassr) for Chemical Exchange Saturation Transfer (Cest) Experiments. *Magn. Reson. Med.* **2009**, *61*, 1441–1450. [CrossRef]
52. Schuenke, P.; Windschuh, J.; Roeloffs, V.; Ladd, M.E.; Bachert, P.; Zaiss, M. Simultaneous Mapping of Water Shift and B1 (Wasabi)-Application To Field-Inhomogeneity Correction of Cest MRI Data. *Magn. Reson. Med.* **2017**, *77*, 571–580. [CrossRef]
53. Schmitt, B.; Zaiß, M.; Zhou, J.; Bachert, P. Optimization of pulse train presaturation for CEST imaging in clinical scanners. *Magn. Reson. Med.* **2011**, *65*, 1620–1629. [CrossRef]
54. Roeloffs, V.; Meyer, C.; Bachert, P.; Zaiss, M. Towards quantification of pulsed spinlock and CEST at clinical MR scanners: An analytical interleaved saturation-relaxation (ISAR) approach. *NMR Biomed.* **2014**, *28*, 40–53. [CrossRef] [PubMed]
55. Zaiss, M.; Angelovski, G.; Demetriou, E.; McMahon, M.T.; Golay, X.; Scheffler, K. QUESP and QUEST revisited—Fast and accurate quantitative CEST experiments. *Magn. Reson. Med.* **2017**, *79*, 1708–1721. [CrossRef] [PubMed]
56. Wada, T.; Togao, O.; Tokunaga, C.; Funatsu, R.; Yamashita, Y.; Kobayashi, K.; Nakamura, Y.; Honda, H. Glycosaminoglycan chemical exchange saturation transfer in human lumbar intervertebral discs: Effect of saturation pulse and relationship with low back pain. *J. Magn. Reson. Imaging* **2016**, *45*, 863–871. [CrossRef] [PubMed]
57. Agarwal, V.; Linser, R.; Fink, U.; Faelber, K.; Reif, B. Identification of Hydroxyl Protons, Determination of Their Exchange Dynamics, and Characterization of Hydrogen Bonding in a Microcrystallin Protein. *J. Am. Chem. Soc.* **2010**, *132*, 3187–3195. [CrossRef] [PubMed]
58. Wilms, L.M.; Radke, K.L.; Abrar, D.B.; Latz, D.; Schock, J.; Frenken, M.; Windolf, J.; Antoch, G.; Filler, T.J.; Nebelung, S. Micro- and Macroscale Assessment of Posterior Cruciate Ligament Functionality Based on Advanced MRI Techniques. *Diagnostics* **2021**, *11*, 1790. [CrossRef]
59. Ishikawa, T.; Watanabe, A.; Kamoda, H.; Miyagi, M.; Inoue, G.; Takahashi, K.; Ohtori, S. Evaluation of Lumbar Intervertebral Disc Degeneration Using T1ρ and T2 Magnetic Resonance Imaging in a Rabbit Disc Injury Model. *Asian Spine J.* **2018**, *12*, 317–324. [CrossRef]
60. Waltz, R.; Morales, J.; Nocedal, J.; Orban, D. An interior algorithm for nonlinear optimization that combines line search and trust region steps. *Math. Program.* **2006**, *107*, 391–408. [CrossRef]
61. Masnadi-Shirazi, H.; Mahadevan, V.; Vasconcelos, N. On the design of robust classifiers for computer vision. In Proceedings of the 2010 IEEE Computer Society Conference on Computer Vision and Pattern Recognition, San Francisco, CA, USA, 13–18 June 2010; pp. 779–786.
62. Yushkevich, P.A.; Piven, J.; Hazlett, H.C.; Smith, R.G.; Ho, S.; Gee, J.C.; Gerig, G. User-guided 3D active contour segmentation of anatomical structures: Significantly improved efficiency and reliability. *NeuroImage* **2006**, *31*, 1116–1128. [CrossRef]
63. Cohen, J. *Statistical Power Analysis for the Behavioral Sciences*; Routledge: London, UK, 2013.
64. Koo, T.K.; Li, M.Y. A Guideline of Selecting and Reporting Intraclass Correlation Coefficients for Reliability Research. *J. Chiropr. Med.* **2016**, *15*, 155–163. [CrossRef]
65. Shrout, P.E.; Fleiss, J.L. Intraclass Correlations: Uses in Assessing Rater Reliability. *Psychol. Bull.* **1979**, *86*, 420–428. [CrossRef]
66. Armstrong, R.A. When to Use the Bonferroni Correction. *Ophthalmic Physiol. Opt.* **2014**, *34*, 502–508. [CrossRef] [PubMed]
67. Mougin, O.; Clemence, M.; Peters, A.; Pitiot, A.; Gowland, P. High-resolution imaging of magnetisation transfer and nuclear Overhauser effect in the human visual cortex at 7 T. *NMR Biomed.* **2013**, *26*, 1508–1517. [CrossRef] [PubMed]

68. Shah, S.M.; Mougin, O.E.; Carradus, A.J.; Geades, N.; Dury, R.; Morley, W.; Gowland, P.A. The z-spectrum from human blood at 7T. *NeuroImage* **2017**, *167*, 31–40. [CrossRef] [PubMed]
69. Singh, A.; Debnath, A.; Cai, K.; Bagga, P.; Haris, M.; Hariharan, H.; Reddy, R. Evaluating the feasibility of creatine-weighted CEST MRI in human brain at 7 T using a Z-spectral fitting approach. *NMR Biomed.* **2019**, *32*, e4176. [CrossRef] [PubMed]